

***WEST ANTARCTIC ICE SHEET CLOUD COVER AND
SURFACE RADIATION BUDGET FROM NASA A-TRAIN
SATELLITES***

Scott, R. C., Lubin, D., Vogelmann, A. M., and Kato, S.

*Accepted for publication in
Journal of Climate*

May 2017

**Environmental & Climate Science Dept.
Brookhaven National Laboratory**

**U.S. Department of Energy
DOE Office of Science**

Notice: This manuscript has been authored by employees of Brookhaven Science Associates, LLC under Contract No. DE-SC0012704 with the U.S. Department of Energy. The publisher by accepting the manuscript for publication acknowledges that the United States Government retains a non-exclusive, paid-up, irrevocable, world-wide license to publish or reproduce the published form of this manuscript, or allow others to do so, for United States Government purposes.

This preprint is intended for publication in a journal or proceedings. Since changes may be made before publication, it may not be cited or reproduced without the author's permission.

DISCLAIMER

This report was prepared as an account of work sponsored by an agency of the United States Government. Neither the United States Government nor any agency thereof, nor any of their employees, nor any of their contractors, subcontractors, or their employees, makes any warranty, express or implied, or assumes any legal liability or responsibility for the accuracy, completeness, or any third party's use or the results of such use of any information, apparatus, product, or process disclosed, or represents that its use would not infringe privately owned rights. Reference herein to any specific commercial product, process, or service by trade name, trademark, manufacturer, or otherwise, does not necessarily constitute or imply its endorsement, recommendation, or favoring by the United States Government or any agency thereof or its contractors or subcontractors. The views and opinions of authors expressed herein do not necessarily state or reflect those of the United States Government or any agency thereof.

West Antarctic Ice Sheet cloud cover and surface radiation budget from

NASA A-Train satellites

Ryan C. Scott* and Dan Lubin

Scripps Institution of Oceanography, La Jolla, California

Andrew M. Vogelmann

Brookhaven National Laboratory, Upton, New York

Seiji Kato

NASA Langley Research Center, Hampton, Virginia

*Corresponding author address: Scripps Institution of Oceanography, 9500 Gilman Drive, MC

0208, La Jolla, CA, USA

E-mail: rscott@ucsd.edu

ABSTRACT

Clouds are an essential parameter of the surface energy budget influencing the West Antarctic Ice Sheet (WAIS) response to atmospheric warming and net contribution to global sea-level rise. A four-year record of NASA A-Train cloud observations is combined with surface radiation measurements to quantify the WAIS radiation budget and constrain the three-dimensional occurrence frequency, thermodynamic phase partitioning, and surface radiative effect of clouds over West Antarctica (WA). The skill of satellite-modeled radiative fluxes is confirmed through evaluation against measurements at four Antarctic sites (WAIS Divide Ice Camp, Neumayer, Syowa, and Concordia Stations). Due to perennial high-albedo snow and ice cover, cloud infrared emission dominates over cloud solar reflection/absorption leading to a positive net all-wave cloud radiative effect (CRE) at the surface, with all monthly means and 99.15% of instantaneous CRE values exceeding zero. The annual-mean CRE at the WAIS surface is 34 W m^{-2} , representing a significant cloud-induced warming of the ice sheet. Low-level liquid-containing clouds, including thin liquid water clouds implicated in radiative contributions to surface melting, are widespread and most frequent in WA during the austral summer. In summer, clouds warm the WAIS by 26 W m^{-2} , on average, despite maximum offsetting shortwave CRE. Glaciated cloud systems are strongly linked to orographic forcing, with maximum incidence on the WAIS continuing downstream along the Transantarctic Mountains.

33 **1. Introduction and Motivation**

34 Antarctica contains the largest reservoir of ice on Earth. Clouds modulate this reservoir by
35 linking poleward energy and water vapor transport to precipitation and by perturbing the energy
36 budget governing the melting and sublimation of snow and ice. By altering the net surface radiative
37 flux, clouds have the ability to alter the onset, extent, intensity, and duration of surface melting
38 and subsequent refreezing, thereby exerting an essential control on meltwater's ability to impact
39 cryospheric dynamics or run-off into the ocean (van Tricht et al. 2016). However, despite their
40 first-order influence on fluctuations in ice sheet volume and global sea-level, Antarctic clouds
41 have received minimal scientific attention over the last several decades (Bromwich et al. 2012;
42 Scott and Lubin 2016).

43 While the relatively high, cold, and massive East Antarctic Ice Sheet is thought to be relatively
44 stable and potentially gaining mass through excess snowfall (Shepherd et al. 2012; Zwally et al.
45 2015), the lower-lying marine WAIS is currently losing mass (-65 ± 26 Gt/yr) at an accelerating
46 rate, contributing to global sea-level rise (Shepherd et al. 2012; Kopp et al. 2016). In contrast
47 to the Greenland Ice Sheet (GrIS), where mass loss is dominated by atmospheric forcing of the
48 surface energy balance (Enderlin et al. 2014; van den Broeke et al. 2016), ice loss from WA to
49 date primarily results from the inflow of warm subsurface water masses onto the continental shelf,
50 and rapid melting at the base of coastal ice shelves (Paolo et al. 2015). While ice shelf thinning,
51 tributary glacier acceleration, and grounding line retreat in the Amundsen Sea Embayment likely
52 manifest the early stages of long-hypothesized (Mercer 1978) marine ice sheet instability (Joughin
53 et al. 2014; Rignot et al. 2014), air temperatures over central WA have increased rapidly over the
54 last several decades (Reusch and Alley 2004; Johanson and Fu 2007; Schneider and Steig 2008;
55 Barrett et al. 2009; Orsi et al. 2012; Abram et al. 2013; Bromwich et al. 2013; Steig et al. 2013;

56 Thomas et al. 2013, 2015; Nicolas and Bromwich 2014). Previous studies attribute this warming to
57 an increasing marine influence on the climate of WA, traceable to large-scale climate oscillations
58 and decadal variability in the tropics and subtropics (Schneider and Steig 2008; Schneider et al.
59 2012; Bromwich et al. 2013; Steig et al. 2013; Nicolas and Bromwich 2014; Thomas et al. 2015),
60 yet an increasing influence from marine airmasses implies a changing surface energy balance (Das
61 and Alley 2008) with an increasing importance of cloud radiative effects.

62 The first spaceborne active-sensor analysis of cloud cover atop the Antarctic ice sheets was en-
63 abled by NASA's 2003 launch of the Ice, Cloud, and land Elevation Satellite (ICESat). In ICESat
64 data from October 2003, Spinhirne et al. (2005) found distinctly greater cloud cover over West
65 (versus East) Antarctica, with a tongue of enhanced cloudiness stretching inland from the Amund-
66 sen Sea. Using high-resolution numerical weather forecasts evaluated against satellite lidar mea-
67 surements, Nicolas and Bromwich (2011) demonstrate that this cloud band is a dominant feature
68 of the climate of WA linked to persistent inflow of oceanic air induced by semipermanent low pres-
69 sure and clockwise flow over the Ross and Amundsen Seas. Annual mean maps reveal co-located
70 bands of enhanced cloud fraction, snow accumulation, and 2-m potential temperature stretching
71 from the Amundsen Sea coastal region to the southern Ross Ice Shelf. To further advance our
72 understanding of the West Antarctic climate, it is essential to characterize the macrophysical and
73 microphysical structure of these cloud systems and their impact on the WAIS surface energy bud-
74 get. This is particularly important in light of especially rapid, widespread atmospheric warming in
75 austral spring (Nicolas and Bromwich 2014) leading into the summer melt season, which has been
76 linked to a deepening of the Amundsen Sea Low (Bromwich et al. 2013; Raphael et al. 2016).
77 However, owing to the high uncertainties associated with passive cloud detection over snow/ice
78 and a scarcity of in situ observations, the microphysical structure and radiative impact of clouds
79 over WA remain largely unexplored.

80 As temperatures rise, GCM simulations project increases in surface melt and snow accumulation
81 (Trusel et al. 2015; DeConto and Pollard 2016; Frieler et al. 2015; Lenaerts et al. 2016), with each
82 exerting competing influences on the ice mass balance. Changes in cloud amount and cloud optical
83 properties due to shifts in the atmospheric circulation or thermodynamic state have the potential to
84 substantially alter surface radiative fluxes, thereby accelerating or mitigating WAIS contributions
85 to global sea-level rise. Indeed, model calculations (Zhang et al. 1996) and polar field observa-
86 tions (Bennartz et al. 2013; Niwano et al. 2015; Tjernström et al. 2015; Nicolas et al. 2017) reveal
87 that cloud radiative effects often provide a significant fraction of the energy used in melting the
88 surface. Nevertheless, poor model representations of clouds and radiation undermine the fidelity
89 of the ice energy balance simulated by the most sophisticated and high-resolution models. An
90 especially common problem is insufficient cloud liquid simulated at supercooled temperatures,
91 which yields radiant flux biases including excessive incident solar energy and insufficient radia-
92 tively opaque states in the infrared (IR) (Klein et al. 2009; Cesana et al. 2012). King et al. (2015)
93 report large errors in the summer surface energy budget and surface melt rates on the Larsen C
94 Ice Shelf simulated by three widely-used regional atmospheric models and emphasize the need
95 to improve observational constraints on Antarctic cloud microphysical and radiative properties.
96 Thus, significant uncertainty remains as to whether cloud processes will contribute to enhanced
97 WAIS mass loss, as appears to be the case in Greenland (Bennartz et al. 2013; Niwano et al. 2015;
98 van Tricht et al. 2016), or whether increased accumulation (Thomas et al. 2015; Fudge et al. 2016)
99 might be sufficient to offset an inherently unstable, oceanically-triggered ice sheet collapse.

100 Due to its strong influence on cloud optical depth and IR emissivity, liquid-bearing clouds are
101 known to play a major and often dominant role in the polar surface energy balance (Shupe and
102 Intrieri 2004). When temperatures approach the melting point, especially important are geomet-
103 rically and optically thin, low-level liquid water clouds containing a liquid water path (LWP)

104 sufficiently small to remain transmissive to solar radiation, yet radiate essentially as a blackbody
105 in the IR. Using a simple surface energy balance model with cloud and radiation measurements
106 at Summit, Greenland (Shupe et al. 2013), Bennartz et al. (2013) implicate such clouds in pro-
107 moting and maintaining temperatures above 0°C during the extreme GrIS melt episode of July
108 2012 (?). Niwano et al. (2015) corroborate the importance of cloud radiative effects in this melt
109 event using a sophisticated snowpack model with radiative fluxes observed in the northwestern
110 GrIS ablation zone. In the East Siberian Sea, Tjernström et al. (2015) also observed thin, warm
111 clouds/fog that were transmissive to sunlight and drove positive net longwave radiation at the sur-
112 face, with the combined effects constituting a potent atmospheric forcing causing rapid top-down
113 sea-ice loss. Indeed, Miller et al. (2015) report that thin clouds with a LWP between 10-40 g m⁻²
114 exert the strongest surface warming effect of all cloud scenes observed atop the central GrIS. They
115 also demonstrate that ice clouds can exert a substantial surface warming effect, especially when
116 geometrically and optically thick, and thus emissive, in the IR. Together, these studies motivate
117 questions regarding the distribution and phase of clouds over WA.

118 Of particular concern as temperatures rise is the susceptibility of the WAIS and fringing ice
119 shelves to the formation of supraglacial melt ponds. Surface meltwater threatens ice sheet integrity
120 via its ability to alter ice flow dynamics (Zwally et al. 2002; Das et al. 2008), the thermomechanical
121 properties of glacial ice (Bell et al. 2014), and by precipitating the catastrophic disintegration of
122 ice shelves constraining the flow of grounded continental ice streams (Scambos et al. 2000, 2004;
123 Rignot et al. 2004; van den Broeke 2005). Meltwater percolation to the ice-bedrock interface in
124 Greenland has been observed to enhance outlet glacier and ice sheet flow via basal lubrication
125 (Zwally et al. 2002; Das et al. 2008), and to create warm basal ice units that flow more readily
126 than cold, unaltered glacial ice (Bell et al. 2014). Although meltwater impacts on cryospheric
127 dynamics to date remain largely confined to Greenland and the Antarctic Peninsula, microwave

128 signatures of surface melt are observed in the present climate on vast low-lying portions of the
129 WAIS and fringing ice shelves (Nghiem et al. 2007; Tedesco et al. 2007). One of the largest melt
130 events on record occurred in January 2016 in response to an advective impulse of cloudy marine
131 air, as described by Nicolas et al. (2017). Increases in surface melt extent, frequency, and volume
132 have led the GrIS to become a dominant contributor to global sea-level rise (van den Broeke et al.
133 2016), but it remains to be seen whether the WAIS will experience a similar fate.

134 In this study, we quantify the three-dimensional occurrence frequency, thermodynamic phase
135 partitioning, and surface radiative impact of clouds over WA. We combine ground-based radiation
136 measurements with cloud observations acquired by the NASA A-Train CloudSat Cloud Profiling
137 Radar (CPR) (Stephens et al. 2002) and Cloud-Aerosol Lidar and Infrared Pathfinder Satellite
138 Observations (CALIPSO) Cloud-Aerosol Lidar with Orthogonal Polarization (CALIOP) (Winker
139 et al. 2009) during 2007-2010, when satellite data are available in co-located form. Section 2
140 describes the satellite cloud and surface radiation measurements and evaluates the performance of
141 satellite-modeled radiative fluxes. Section 3 examines the distribution and phase of clouds over
142 the WAIS and major ice shelves (Ross and Ronne-Filchner) and their linkages with the prevailing
143 regional meteorology. Sections 4 and 5 present the annual cycles in net surface radiative fluxes
144 and cloud radiative effects over the grounded WAIS, and at the WAIS Divide Ice Camp (Fig. 1).
145 This location is the site of the WAIS Divide ice core and more recently the Atmospheric Radiation
146 Measurement (ARM) West Antarctic Radiation Experiment (AWARE), a comprehensive atmo-
147 spheric observation campaign that took place during the 2015-2016 austral summer field season
148 (Nicolas et al. 2017). Section 6 summarizes and discusses the results.

2. Data and Methods

a. NASA A-Train Satellite Observations

The NASA A-Train CloudSat and CALIPSO satellites provide high-resolution nadir vertical profiles of clouds, offering unprecedented insight into the vertical distribution and internal structure of Antarctic cloud systems. Operating at 3.2 mm, the CPR probes thick clouds with high sensitivity to the presence of ice crystals in mixed-phase clouds. CALIOP, the first spaceborne depolarization lidar, readily penetrates optically thin clouds and discriminates ice from liquid-bearing cloud layers. Due to their narrow swaths, spatial sampling is limited to along the satellite track. Their orbits converge toward a poleward observational limit at 82°S, providing 7-8 overpasses intersecting the WAIS each day. Nonetheless, the ability of these instruments to produce accurate and extensive cloud data provides a powerful tool to assess cloud properties and impacts on the West Antarctic climate and energy budget.

Analysis of cloud structure and phase over WA is performed using the CloudSat-CALIPSO 2B-CLDCLASS-LIDAR cloud mask (Zhang et al. 2010; Wang et al. 2013). 2B-CLDCLASS-LIDAR takes advantage of the unique signatures of ice crystal and liquid droplet populations at the radar and lidar operational wavelengths to retrieve the thermodynamic phase of all hydrometeor layers in each co-located radar-lidar profile. In general, high backscatter, rapid extinction, and minimal depolarization of the lidar signal provide a classic indicator of the presence of cloud liquid, whereas the opposite is true for ice. Mixed-phase clouds are distinguished from liquid water clouds using a temperature-based radar reflectivity threshold whereby higher reflectivities indicate the presence of ice (Wang et al. 2013). The absence of ground- and/or aircraft-based cloud observations over Antarctica during the study period (2007-2010) unfortunately precludes validation of the 2B-CLDCLASS-LIDAR algorithm; however, as shown in Table 1, a high percentage of cloud phase

retrievals have high confidence (Wang et al. 2013) over Antarctica and the Southern Ocean pole-ward of 60°S. Radar-lidar measurements readily discriminate single-phase clouds and less than 7% of mixed-phase retrievals are considered uncertain in each season. Here, with minimal bearing on the results, we retain and interpret this small percentage of cases to represent mixed-phase clouds.

The two-dimensional cloud frequency, or cloud amount, is computed as

$$CFreq(i, j) = \frac{1}{N(i, j)} \sum_{p=1}^{N(i, j)} n_{p, cloud}(i, j), \quad (1)$$

where N depicts the number of satellite profiles in 2° latitude-longitude grid cell (i, j) , and $n_{p, cloud} = 1$ if cloud is detected in the atmospheric column (otherwise $n_{p, cloud} = 0$). The three-dimensional cloud frequency, hereafter referred to as cloud incidence, is computed on monthly and seasonal time scales for ice, mixed-phase, and liquid water clouds using the following procedure. First, we discretize the Antarctic atmosphere into three-dimensional volumes having 2° latitude-longitude by 240-m vertical resolution. When CloudSat-CALIPSO observe a cloud layer we increment by unity all atmospheric volumes containing the cloud. All atmospheric volumes are then normalized by the total number of (clear plus cloudy) satellite profiles in each grid cell. Thus, a mixed-phase cloud incidence of 0.25, for example, indicates that cloud containing supercooled liquid droplets and ice crystals was observed 25% of the time. Note that this method differs from the one employed by Verlinden et al. (2011).

To quantify the ice sheet radiation budget and the radiative impact of clouds, we estimate surface radiative fluxes using the Clouds and the Earth's Radiant Energy System (CERES) CALIPSO-CloudSat-CERES-MODIS (C3M) data set (Kato et al. 2010, 2011). Cloud radiative impacts at the surface are quantified by calculating the cloud radiative forcing (Ramanathan et al. 1989), or

cloud radiative effect (CRE), defined as the difference between all-sky and otherwise equivalent clear-sky surface radiative fluxes. We compute the longwave, shortwave, and all-wave CRE as

$$CRE_{LW} = F_L(A_c) - F_L(0), \quad (2)$$

$$CRE_{SW} = F_S(A_c) - F_S(0), \quad (3)$$

$$CRE = CRE_{LW} + CRE_{SW}, \quad (4)$$

where F_L and F_S represent the net longwave and shortwave surface radiative fluxes, and A_c represents the fractional cloud cover along the active sensor ground track, as discussed below. The longwave CRE is typically positive since clouds absorb and emit IR radiation more efficiently than the clear atmosphere, thereby enhancing the downwelling IR flux. The shortwave CRE is typically negative as clouds attenuate incoming solar radiation via scattering and absorption. A positive all-wave CRE indicates enhanced net radiation at the surface with the presence of clouds, and vice versa.

C3M provides longwave (4-50 μm) and shortwave (0.2-4 μm) fluxes along the narrow active sensor ground track computed using the Flux model for CERES with k-distribution and correlated-k for Radiation (FLCKKR) two-stream radiative transfer model. The atmospheric state is specified using temperature, pressure, water vapor, and ozone profiles from Goddard Earth Observing System version 5 (GEOS-5) reanalyses. Clear-sky fluxes account for scattering and absorption by atmospheric gases only. All-sky fluxes are computed using cloud properties observed by CALIPSO, CloudSat, and Aqua MODIS. C3M cloud boundaries are derived from the CALIPSO Vertical Feature Mask (VFM, 30 m vertical resolution below 8.2 km, 60 m above) and the CloudSat Cloud Classification product (2B-CLDCLASS, 240 m vertical resolution) at 1 km horizontal resolution, closely maintaining the vertical resolution of each product (Kato et al. 2010). Given CALIOP's

214 higher resolution and superior ability to detect cloud-size particles, the CALIPSO VFM provides
215 most cloud boundaries. When the lidar signal fully attenuates, as often occurs in liquid-topped
216 mixed-phase clouds, CPR cloud boundaries are used for clouds detected below the lidar atten-
217 uation level. CALIOP-detected cloud optical properties are derived from the 532-nm extinction
218 profile. When CPR cloud boundaries are used, cloud optical properties are derived from CPR
219 retrievals of cloud ice and liquid water content and effective particle radii from the CloudSat
220 radar-only Cloud Water Content product (2B-CWC-RO). As outlined in Kato et al. (2010, 2011),
221 merged radar-lidar cloud profiles are co-located with Aqua MODIS radiance pixels, which provide
222 an additional constraint on the vertically integrated cloud optical depth. Merged cloud profiles are
223 then grouped and averaged over near-nadir Aqua CERES FM3 footprints (~ 20 km), the scale at
224 which radiative fluxes are computed. All-sky fluxes represent the average of fluxes computed for
225 clear and cloudy skies weighted by the clear and cloud fractions over the CERES footprint, thereby
226 accounting for the effects of fractional cloudiness along the active sensor ground track. Over WA,
227 irradiance calculations use a snow surface broadband emissivity (0.98) and spectral albedo from
228 the MODIS Terra and Aqua 16-day BRDF/Albedo product (MCD43). Rigorous evaluation against
229 in situ data on the GrIS suggests that the MODIS-derived snow albedos are physically realistic
230 (Stroeve et al. 2013). To account for enhancement of the surface albedo due to preferential cloud
231 absorption in the near-IR, the all-sky albedo is computed as the average of clear-sky and overcast
232 albedos weighted by the clear and cloud fractions.

233 *b. Evaluation of C3M radiative fluxes over Antarctica*

234 As one of the most remote and inhospitable locations on Earth, WA has for decades been devoid
235 of reliable long-term surface radiation measurements. Nonetheless, three stations representing
236 maritime and continental Antarctic climates relevant to the WAIS, all participating in the Baseline

237 Surface Radiation Network (BSRN) (Ohmura et al. 1998), enable an assessment of the skill of
 238 satellite-modeled surface radiative fluxes. Due to the prolonged absence of sunlight, low solar
 239 incidence angles, and extensive high-albedo snow/ice cover, the Antarctic surface radiation bud-
 240 get is dominated by longwave fluxes for much of the year (Town et al. 2005). Here we evaluate
 241 the performance of C3M all-sky downwelling longwave irradiances against shaded Eppley Preci-
 242 sion Infrared Radiometer (PIR) pyrgeometer measurements at Neumayer, Syowa, and Concordia
 243 Stations (Fig. 1). Measurements cover the spectral interval 4-50 μm and have a manufacturer-
 244 estimated uncertainty of 5 W m^{-2} . Neumayer Station (70.65°S , 8.25°W) is located on the Ek-
 245 ström Ice Shelf in the northeastern Weddell Sea. Syowa Station (69.01°S , 39.59°E) is located on
 246 East Ongul Island in the coastal escarpment of Queen Maud Land. Concordia Station (75.10°S ,
 247 123.38°E), also known as Dome C, sits 3,233 m above mean sea-level (MSL) in the interior of the
 248 East Antarctic Ice Sheet (EAIS).

249 Following the Arctic evaluation of C3M downwelling longwave fluxes presented by Kato et al.
 250 (2011), we compare the mean flux over all satellite footprints within 100 km of each site to the
 251 measured flux averaged over 15 minutes at the satellite overpass time. Fig. 2 shows scatterplots
 252 of the modeled versus measured downwelling longwave radiation along with histograms of the
 253 instantaneous irradiance error, defined as the modeled minus the measured flux. Statistics pre-
 254 sented include the mean bias (Δ), root-mean-square error (RMSE), and Pearson linear correlation
 255 coefficient (r). Table 2 summarizes the results resolved by site and season.

256 Larger longwave irradiances occur in the relatively warm and moist coastal atmospheres. At the
 257 coastal sites, C3M exhibits a tendency to underestimate the true flux, with mean biases of -5.1
 258 and -9.7 W m^{-2} (Fig. 2). As evidenced by the regression lines, C3M transitions from typically
 259 overestimating to underestimating the mean downwelling longwave radiation near 200 W m^{-2} .
 260 Simulated fluxes are nonetheless positively correlated with measurements at both sites, with Neu-

261 mayer showing the strongest correlation. Instantaneous irradiance errors, while mostly smaller
262 than 50 W m^{-2} at Neumayer, tend toward larger negative values at Syowa, which also shows the
263 weakest correlation and largest RMSE. Within 100 km of Syowa, the EAIS rises up to 1,450 m
264 above MSL introducing noise in the comparison of point measurements with satellite fluxes av-
265 eraged over 100 km radius. Filtering out footprints over the EAIS from the comparison increases
266 the correlation to 0.67, decreases the RMSE to 34.7, and reduces the mean bias to -0.5 W m^{-2} .

267 Clouds are considerably less frequent on the Antarctic Plateau, where ice clouds comprise the
268 dominant cloud type (not shown); however, we note that CloudSat-CALIPSO reveals mixed-phase
269 clouds over the EAIS during summer consistent with ground-based cloud observations at Princess
270 Elizabeth (Gorodetskaya et al. 2015) and Amundsen-Scott South Pole Stations (Lawson and Get-
271 telman 2014). Concordia's prominent irradiance error mode at 0 W m^{-2} reveals frequent close
272 agreement between modeled and measured fluxes. In contrast to the coastal sites, the modeled
273 downwelling longwave radiation at Concordia is biased by 12.1 W m^{-2} , on average, as evidenced
274 by the irradiance error distribution positive skew. The lower cloud amounts and concentration of
275 data points at small irradiances suggest clear-sky origins related to occasional errors in the temper-
276 ature and moisture profiles that dominate the C3M downwelling longwave radiation uncertainty
277 (Kato et al. 2011, 2012).

278 Considering all sites together, the C3M downwelling longwave radiation is strongly correlated (r
279 $= 0.9$) with BSRN measurements. Together with a small mean bias of -1.02 W m^{-2} , these results
280 reveal high skill in the C3M-simulated downwelling longwave radiation. If footprints around
281 Syowa over the EAIS are filtered out, the all-site mean bias changes to 2.27 W m^{-2} , with minor
282 improvements to the correlation and RMSE. Interestingly, a similar level of agreement was found
283 over three Arctic sites (Kato et al. 2011), indicating comparable performance over both polar

regions. A similar exercise for the upwelling longwave radiation at the coastal stations (where data are available) yields similar results, with an all-site $\Delta = -1.5 \text{ W m}^{-2}$ and $r = 0.76$.

The downwelling shortwave radiation was also measured at these sites by Kipp and Zonen pyranometers covering the spectral interval 0.285-2.8 μm . The manufacturer-estimated measurement uncertainty is 3% of the incident solar radiation. An instantaneous downwelling shortwave comparison was difficult to make, however, owing to disparities in the satellite-sensor and surface-radiometric viewing geometries, greater sensitivity of the incoming shortwave radiation to 3D radiative transfer effects, and potential cosine response measurement errors. Table 3 instead presents statistics for a comparison of the monthly-mean downwelling longwave and shortwave fluxes. Results for the longwave closely resemble the instantaneous comparison (Fig. 2) but show slight overall improvements to the statistics. Shortwave correlations are strong and positive but the biases and RMSEs are slightly lower in quality. On the monthly time scale, we find that C3M underestimates the all-site downwelling shortwave radiation by an average of 13.2 W m^{-2} .

c. AWARE Radiation Measurements

From 4 December 2015 to 18 January 2016, the AWARE campaign conducted the first comprehensive suite of surface energy balance, cloud, and upper-air measurements made to date in central WA. An ARM Mobile Facility was deployed to the WAIS Divide Ice Camp (79.467°S, 112.085°W) located 1,801 m above MSL at the summit of the Ross-Amundsen ice divide (Fig. 1). Broadband radiative fluxes were measured by an ARM Sky Radiometer suite (SKYRAD) and a Surface Energy Balance System (SEBS). The downwelling longwave radiation was measured by a pair of shaded Eppley PIR pyrgeometers. Direct and diffuse components of the downwelling shortwave radiation were measured, respectively, by a Normal-Incidence Pyrheliometer and a shaded Black and White Pyranometer. The downwelling shortwave radiation is computed as the sum

307 of the direct component, weighted by the cosine of the SZA, and the diffuse component. Both
308 upwelling fluxes were measured by the SEBS.

309 The AWARE deployment notably took place during a period of high global-average tempera-
310 tures with a record El Niño event in the Pacific Ocean (Nicolas et al. 2017). Although the meteoro-
311 logical conditions at WAIS Divide potentially differ during the satellite and AWARE observation
312 periods, these measurements enable the first direct characterization of the surface radiation budget
313 in central WA. To further assess the reliability of our WAIS radiation climatology, we also com-
314 pare satellite-modeled and measured radiative fluxes at WAIS Divide. Satellite estimates account
315 for all footprints in the four nearest 2° grid cells centered over the site.

316 **3. Results**

317 *a. Satellite Cloud Climatology over WA*

318 Fig. 3 presents the seasonal cloud amount over WA with vectors of the mean horizontal circula-
319 tion at 700-mb from the ERA-Interim reanalysis (Dee et al. 2011). Note that this figure accounts
320 for all detected clouds, providing a close approximation to the time-mean areal cloud fraction. Ad-
321 ditional meteorological context is provided by Fig. 4, showing seasonal composites of the minus
322 pressure vertical velocity at 700-mb (positive values indicate upward motion). Figs. 5-7 present
323 zonal transects centered on 77, 79, and 81°S illustrating the vertical distribution and thermody-
324 namic phase partitioning of this cloud cover.

325 The climatological West Antarctic marine cloud band, most prominent from autumn to spring,
326 consists primarily of geometrically thick ice cloud systems generated through orographic lifting.
327 Indeed, the WAIS experiences greater total cloud cover in seasons with frequent ice clouds linked
328 to prevailing northeasterly-to-northerly upslope flow over the Ross-Amundsen ice divide. Re-

duced cloud amounts occur in the lee of the MBL ice cap, where subsidence and downslope flow promote adiabatic warming and drying of the lower troposphere (Figs. 3-4). Along with outflow and descent of continental air to the east of the central ice divide, this effect acts to sharpen the orographic marine cloud band (Nicolas and Bromwich 2011). In winter, strong meridional inflow and rapid orographic lifting sustains a core of maximum ice cloud incidence that penetrates far inland, dominating cloudiness over the ice sheet (Figs. 3-7d). While ice clouds also dominate in the transitional seasons, low-level mixed-phase clouds comprise a significant fraction of the total cloud cover, especially in autumn near the coast (Figs. 5-6c). In summer, when offshore cyclonic activity weakens and shifts toward the Bellingshausen Sea (Nicolas and Bromwich 2011), weak terrain-parallel flow and weak orographic lifting prevails, yielding a summer ice cloud minimum over the ice sheet (Figs 4-6b). Interestingly, the seasonality of poleward flow and orographic lifting explains why the seasonal cloud incidence exhibits the largest amplitude over the high ice sheet terrain, as noticed by Verlinden et al. (2011).

After traversing the Ross-Amundsen ice divide, the mean 700-mb flow deposits onto the southern Ross Ice Shelf (RIS) in the Siple Coast confluence zone (Parish and Bromwich 1987), producing a strong meteorological connection between the WAIS and the RIS. Southerly advection and rapid ascent along the western RIS and Transantarctic Mountains supports frequent ice and mixed-phase cloud formation downstream (Figs. 3-7). At Ross Island, the downstream effect of advection from the Amundsen Sea basin is evident in winter-spring as a core of geometrically thick ice clouds (Figs. 5a,d). These cloud systems, extending from the surface to 5-6 km altitude, are closely linked to the Ross Ice Shelf airstream, a prominent low-level jet along the western RIS that shares the same seasonality in terms of size and strength (Seefeldt and Cassano 2008). During the warmer summer-autumn months, cloud systems along the western RIS exhibit a stronger mixed-phase component (Fig. 5b,c). Signatures of these clouds are also seen along the western RIS in

Fig. 3a,c, where slightly greater cloud amounts are observed relative to the central RIS. These results extend previous observations of geometrically thick ice-dominant cloud systems arriving at Ross Island from the Antarctic interior (Scott and Lubin 2014).

Liquid-containing clouds undergo a strong seasonal cycle over WA, with the highest frequencies in summer and the lowest in winter (Figs. 5-7). In summer, low mixed-phase clouds dominate the total cloud cover (Fig. 5-7b). Although they are the least frequent cloud type, also widespread are liquid water clouds, which tend to be contrastingly thin and confined near the surface, as observed in the Arctic (Shupe 2011). Liquid water clouds are especially frequent on the RIS (Fig. 5-7b), particularly in December-January (Fig. 8), the months of peak summer warmth in WA. Mixed-phase cloud frequencies maximize in areas of complex terrain (Figs. 7-8), highlighting the importance of orographic updrafts in the formation, persistence, and glaciation of mixed-phase clouds (Scott and Lubin 2016; Lohmann et al. 2016). By contrast, significant reductions in low-level cloud cover are found over the subsidence-prone MBL and Siple Coast region (220-240°E) on monthly and seasonal time scales, especially for mixed-phase clouds (Figs. 5-8).

Although the WAIS is least cloudy in summer (Fig. 3), the reduction in total cloud amount largely reflects the minimum in ice clouds, and is partially compensated by increases in low-level mixed-phase and liquid water cloud cover. The summer maximum in radiatively important liquid-bearing clouds suggests that warmer temperatures, air-sea exchange, and neutral to weakly unstable lower tropospheric stability play a greater role in low cloud formation in central WA than previously realized (Nicolas and Bromwich 2011; Verlinden et al. 2011). Indeed, as summer progresses from December to February (Fig. 8), mixed-phase cloud incidence and geometrical thickness increases rapidly toward an annual maximum in February concurrent with the Antarctic sea-ice minimum (although not shown, the March mixed-phase cloud incidence decreases to December-January levels). Additional intraseasonal cloud variability in Fig. 8 can likely be at-

tributed to variability in the atmospheric circulation (Nicolas and Bromwich 2011). Fig. 8 also provides further evidence that ice clouds typically form in response to orographic lifting rather than simply cold Antarctic temperatures.

b. WAIS Radiation Budget

The radiation budget, or net radiation, at the WAIS surface is given by the sum of net longwave and shortwave radiative fluxes. Fig. 9 presents the annual cycle and monthly variability in net surface radiative fluxes over the entire WAIS and at WAIS Divide. From April to August, the Sun remains below the horizon and the net radiation is exclusively determined by IR fluxes. In these months, the surface-emitted upwelling IR radiation exceeds the downwelling component from the atmosphere, resulting in an average IR energy loss of 16.8 W m^{-2} . The Sun rises in September and remains above the horizon until March. The incoming solar radiation, although largely reflected, is partially absorbed by the ice sheet, primarily at near-IR wavelengths where the surface albedo is low (Grenfell et al. 1994). The net shortwave radiation over the entire WAIS peaks at 74.6 W m^{-2} in December, when solar zenith angles (SZAs) are lowest. Solar absorption increases the ice sheet surface temperature, enhancing the emitted upwelling IR radiation. However, despite increases in air temperature and liquid-bearing cloud cover, the upwelling IR radiation greatly exceeds the downwelling component from the atmosphere, yielding a peak-summer ice-sheet-wide mean IR energy loss of 53.2 W m^{-2} . Solar absorption dominates the mean net radiation from November to February, peaking at 21.4 W m^{-2} in December-January.

Satellite-modeled fluxes at WAIS Divide closely resemble those for the broader WAIS, with minor differences between the domains. Over the entire WAIS, the mean annual cycle, interquartile range, and 95th percentiles in net shortwave radiation exceed those at WAIS Divide. This reflects estimates at lower latitudes, where lower SZAs lead to higher insolation, and lower elevations,

400 where downslope winds increase the atmospheric shortwave transmittance. Notably, the retrieved
401 annual cycle in net radiation at WAIS Divide resembles direct measurements at the South Pole
402 (Town and Walden 2009).

403 Table 4 compares the December-January mean and standard deviation of C3M and AWARE
404 net radiative fluxes at WAIS Divide. Close agreement between the net longwave fluxes further
405 supports C3M's ability to constrain the WAIS longwave radiation budget. Greater variability in
406 simulated fluxes is likely attributed to the wider range of meteorological conditions over the 4-
407 year satellite period than during our 46-day deployment at WAIS Divide. The satellite-modeled
408 net shortwave radiation exceeds AWARE measurements by 7.6 W m^{-2} . This suggests that C3M
409 slightly overestimates surface solar absorption due to a potentially low-biased albedo used in the
410 radiative transfer calculations. Although Stroeve et al. (2013) report good agreement between the
411 MODIS albedo and in situ data on the GrIS, a previous evaluation found it to be biased by -0.05
412 (Stroeve et al. 2005). In the absence of long-term radiation measurements, a similar evaluation of
413 the MODIS-derived surface albedo over the WAIS is currently not possible.

414 At WAIS Divide, the mean net shortwave radiation measured during AWARE (59.25 W m^{-2})
415 exceeds that at Summit, Greenland, where Miller et al. (2015) report a peak-summer value of
416 approximately 55 W m^{-2} . This result is likely attributed to the minimum Earth-Sun distance in
417 January; the eccentricity of the Earth's orbit causes variations in TOA insolation of approximately
418 7% during a year. However, differences in atmospheric shortwave transmittance and/or surface
419 albedo may also play a role.

420 *c. WAIS Cloud Radiative Effects*

421 Fig. 10 presents the annual cycle and monthly variability in surface CRE components over the
422 entire WAIS and at WAIS Divide. The longwave CRE increases with the cloud amount, temper-

423 ature, and emissivity. Due to the relatively uniform high-albedo snow/ice surface, the shortwave
424 CRE primarily depends on cloud transmittance and SZA. It becomes increasingly negative with a
425 decrease in either parameter (Shupe and Intrieri 2004).

426 During the polar night, cloud enhancement of the downwelling longwave radiation warms the
427 WAIS by an average of 38 W m^{-2} . The longwave CRE undergoes a weak mean annual cycle,
428 increasing by 14 W m^{-2} from a winter minimum to a late-summer maximum in January-February
429 due to relatively warm, low-level liquid-containing clouds (Figs. 5-8). The longwave CRE de-
430 creases from February to May as temperatures and liquid-bearing cloud cover decrease and sea-
431 ice begins to expand around the continent. The shortwave CRE is largely driven by insolation
432 and attains a similar maximum in December-January when SZAs are lowest. Nonetheless, the
433 all-wave CRE is positive in 99.15% of instantaneous calculations and for all monthly means, in-
434 dicating that clouds radiatively warm the surface of the WAIS throughout the year. On the annual
435 average, clouds enhance the net radiation at the WAIS surface by 34 W m^{-2} relative to clear skies.
436 Although the longwave CRE maximizes in summer, the all-wave CRE is minimum due to the rela-
437 tively large magnitude of the offsetting shortwave CRE. Averaged over the WAIS during summer,
438 the all-wave CRE is 26 W m^{-2} . As the Sun falls below the horizon, the all-wave CRE exhibits
439 a slight annual maximum in March due to persistent low-level liquid-containing clouds and thick
440 ice clouds.

441 Interestingly, the shortwave CRE annual cycle over WAIS Divide (Fig. 10) exceeds estimates at
442 Summit, Greenland (Miller et al. 2015), by an approximate factor of two. This could result from
443 site differences in cloud microphysical properties determining cloud shortwave transmittance, such
444 as cloud ice and liquid water path (Scott and Lubin 2016), or to biases in the MODIS-derived
445 surface albedo and/or simulated cloud transmission. A low-bias in either parameter would cause
446 an overestimate of the shortwave CRE, translating to a conservative estimate of the all-wave CRE.

447 Since C3M tends to underestimate the incoming all-sky shortwave radiation (Table 3), on average,
448 the net warming influence of clouds may be larger than present estimates suggest, particularly
449 during the sunlit months.

450 Figs. 11-13 present maps revealing spatial variability in the seasonal mean surface CRE com-
451 ponents throughout WA. Spatial patterns in the longwave CRE closely track the cloud amount
452 patterns of Fig. 3. The strongest longwave CRE occurs in summer due to frequent and exten-
453 sive low-level liquid-bearing cloud cover. Outside of summer, the orographic marine cloud band
454 exerts the strongest longwave CRE, particularly atop the Ross-Amundsen and central ice divides.
455 Therefore, the thick ice clouds of Figs. 5-7 substantially increase the downwelling IR radiation
456 at the surface, consistent with recent observations over the GrIS (Miller et al. 2015; van Tricht
457 et al. 2016). Ice and mixed-phase cloud systems also exert distinct longwave and all-wave sur-
458 face radiative signatures downstream along the western RIS (Figs. 11, 13). Regions of prevailing
459 downslope flow and reduced cloud amount experience weaker longwave CRE. Similar longwave
460 CRE patterns are found in the transitional seasons, although larger values occur over Ellsworth
461 Land and the Antarctic Peninsula in spring owing to stronger inflow of marine air and cloudier
462 skies (Fig. 3a,c).

463 The shortwave CRE shows weaker spatial variability owing to the extensive high-albedo
464 snow/ice surface, and the similar albedo of clouds and the underlying surface. Overall, clouds
465 have a weaker ability to cool the surface approaching the pole due to increasing SZA. Liquid-
466 containing clouds, which are more abundant in coastal areas (Figs. 5-7), may also contribute to
467 the latitudinal shortwave CRE gradient through variations in cloud optical thickness. In summer,
468 the low-albedo open ocean enhances the shortwave CRE sufficiently to outweigh the longwave
469 CRE, so that clouds exert a net cooling of the open ocean of up to 60 W m^{-2} (not shown). Note

470 that coastal grid cells with strong shortwave CRE (e.g., along the eastern RIS near Roosevelt
471 Island) occasionally result from averaging footprints over high- and low-albedo surfaces.

472 Spatial patterns in the all-wave CRE closely track the longwave CRE due to the weak latitudinal
473 dependence of the shortwave CRE. The poleward decrease in offsetting shortwave CRE results in a
474 poleward-increasing all-wave CRE in extensively cloudy regions such as the central ice divide. In-
475 deed, the central ice divide experiences the strongest CRE of anywhere in Antarctica equatorward
476 of 82°S, with values exceeding 50 W m⁻² during autumn.

477 **4. Summary and Discussion**

478 The WAIS is likely the single greatest threat to rapid global sea-level rise (Mercer 1978; Joughin
479 et al. 2014; Rignot et al. 2014; DeConto and Pollard 2016). Although warm seawater has been the
480 primary driver of glacial retreat in WA, the surface energy budget is expected to play an increas-
481 ingly important role as the global atmosphere warms (Trusel et al. 2015; DeConto and Pollard
482 2016; Nicolas et al. 2017). How much and how fast the WAIS contributes to sea-level rise will
483 critically depend on how clouds modulate surface energy fluxes and the amount, distribution, and
484 phase of precipitation. However, despite their importance, clouds over WA remain among the least
485 studied and understood of all locations on Earth. Until recently, comprehensive cloud and radiation
486 measurements have remained virtually absent in WA for decades. This has limited our understand-
487 ing of cloud properties and processes over WA and their precise impact on the ice energy and mass
488 budgets. At the same time, the dearth of observations has precluded advances in microphysical
489 parameterizations used to simulate cloud processes in the uniquely cold and pristine Antarctic at-
490 mosphere (Bromwich et al. 2012; King et al. 2015). Thus, it remains poorly understood whether
491 the net effect of clouds will be to accelerate or mitigate WAIS mass loss, contributing to significant
492 uncertainty in global sea-level projections.

Our study advances knowledge of cloud properties over the remote WAIS and highlights the impact of marine air on the surface radiation budget, complementing and extending the work of Nicolas and Bromwich (2011). In particular, we used NASA A-Train satellite observations during 2007-2010 to constrain previously unknown climatological aspects of cloud cover over WA, including its three-dimensional distribution, occurrence frequency, phase partitioning, and surface radiative effects. In conjunction with surface radiation measurements at WAIS Divide and three Antarctic BSRN stations, we evaluated the performance of the satellite-modeled radiative fluxes, providing confidence in our estimates of surface radiative fluxes and cloud radiative effects. Several key findings emerge:

- Through evaluation against BSRN measurements, we find that C3M simulates longwave radiative fluxes over Antarctica with good skill on the instantaneous and monthly time scale. Further confidence in the satellite-modeled radiative fluxes is provided by close agreement with measurements at WAIS Divide during the AWARE campaign. The C3M-simulated downwelling longwave irradiance also exhibits comparable quality over both of the Earth's polar regions (Kato et al. 2011).
- The climatological marine cloud band stretching inland from the Amundsen Sea consists primarily of geometrically thick ice cloud linked to orographic lifting over the eastern Ross-Amundsen ice divide. Ice clouds dominate the total cloud cover over the WAIS from autumn to spring. These cloud systems are a major climatological feature downstream along the western RIS, maintained by low-level ascent forced by the Transantarctic Mountains. The seasonality of this cloud system reflects the seasonality of synoptic activity offshore, which tends to be most intense outside of summer (Nicolas and Bromwich 2011).

- 515 • During summer, low-level mixed-phase clouds dominate the total cloud cover over WA. As

516 summer progresses, mixed-phase cloud incidence increases rapidly toward an annual max-

517 imum in February concurrent with the annual minimum in Antarctic sea-ice extent. These

518 clouds persist through autumn, are least frequent in winter, but become more abundant as

519 temperatures rise in spring. In the continental interior, mixed-phase cloud frequencies maxi-

520 mize in areas of complex terrain, highlighting orographic forcing as an important control on

521 ice-phase microphysics over Antarctica.

- 522 • Geometrically thin liquid water clouds occur at all elevations in WA. They are especially fre-

523 quent at the peak of summer (December-January), particularly on the RIS, suggesting that

524 these clouds can be expected to increase in frequency in a warmer atmosphere. A recent

525 study using AWARE data (Nicolas et al. 2017) confirmed the role of such clouds in enhanc-

526 ing surface energy input during an extensive and prolonged episode of WAIS and RIS surface

527 melting, through the combined transmission of solar radiation and enhancement of down-

528 welling longwave radiation. Nicolas et al. (2017) also show the distribution of cloud LWP

529 at WAIS Divide during this melt event, roughly evenly distributed between the $10\text{-}40\text{ g m}^{-2}$

530 range conducive to the Bennartz et al. (2013) cloud surface radiative enhancement effect, and

531 larger LWPs that produce a dominant blackbody warming effect. AWARE observations, also

532 available at Ross Island, offer an intensive means for investigating the radiative properties of

533 thin liquid water clouds identified here and in Nicolas et al. (2017).

- 534 • Cloud cover warms the WAIS and major ice shelves year-round owing to a dominance of the

535 longwave CRE. The longwave CRE maximizes over the WAIS in summer due to frequent

536 low-level liquid-bearing clouds. However, thick ice cloud systems warm the WAIS for much

537 of the year. The shortwave CRE is limited by extreme SZAs and the highly reflective snow/ice

surface. It becomes increasingly negative from the interior to the coast, where low SZAs prevail and liquid-bearing clouds are more abundant. We estimate that, on average, clouds increase the net surface radiative flux over the WAIS by 34 W m^{-2} relative to clear skies. The net warming influence of clouds is strongest in autumn (MAM) due to minimal insolation (and associated shortwave CRE) and persistent low-level liquid-containing clouds.

- The strongest all-wave CRE occurs over the Amundsen Sea sector of the WAIS, specifically atop the Ross-Amundsen and central ice divides, owing to sustained inflow of warm, cloudy marine airmasses and high SZAs. Regions of prevailing subsidence and downslope flow are associated with reduced cloud amount, and therefore CRE. Ice and mixed-phase cloud systems downstream produce noticeable longwave and all-wave surface radiative signatures along the western RIS.
- The calculated annual-mean CRE over the WAIS is comparable to estimates over the GrIS (Miller et al. 2015; van Tricht et al. 2016) and similar high-albedo Arctic sea-ice surfaces (Intrieri et al. 2002; Shupe and Intrieri 2004). This result is also consistent with a positive correlation found between AIRS-retrieved cloud amount and near-surface air temperature at AWS sites throughout WA (Lubin et al. 2015).

Understanding the precise impact of clouds on the evolution of the WAIS will clearly require intensified effort to monitor and accurately model cloud and radiative processes over the region. The ability of A-Train satellites, and future missions such as EarthCARE (Illingworth et al. 2015), to retrieve vertically-resolved Antarctic cloud properties and surface radiative fluxes with fidelity, as demonstrated here, suggests that satellite remote sensing can play an important role in understanding the WAIS response to a warming global atmosphere.

560 *Acknowledgments.* R.C.S. is supported by the NASA Earth and Space Science Fellowship Pro-
561 gram under NNX15AN45H. The first two authors acknowledge additional support from the U.S.
562 National Science Foundation (NSF) under PLR-1141939. A.M. Vogelmann is supported by U.S.
563 Department of Energy (DOE) grant DE-SC0012704. Thanks to David Rutan of Science Sys-
564 tems and Applications, Inc., for useful discussions and for providing the BSRN surface radia-
565 tion measurements. Valuable comments from three anonymous reviewers helped to improve the
566 manuscript. AWARE is supported by the U.S. DOE ARM Program as an ARM Mobile Facility
567 campaign, and by the U.S. NSF Division of Polar Programs under PLR-1443549. AWARE data are
568 available at the ARM Data Archive (<http://www.arm.gov>). CloudSat-CALIPSO 2B-CLDCLASS-
569 LIDAR and CERES C3M data are available, respectively, from the CloudSat Data Processing Cen-
570 ter (<http://www.cloudsat.cira.colostate.edu/>) and the NASA Langley Atmospheric Science Data
571 Center (<http://eosweb.larc.nasa.gov>).

572 **References**

- 573 Abram, N. J., and Coauthors, 2013: Acceleration of snow melt in an Antarctic Peninsula ice core
574 during the twentieth century. *Nature Geoscience*, **6** (5), 404–411.
- 575 Barrett, B., K. Nicholls, T. Murray, A. Smith, and D. Vaughan, 2009: Rapid recent warming
576 on Rutford Ice Stream, West Antarctica, from borehole thermometry. *Geophysical Research*
577 *Letters*, **36** (2).
- 578 Bell, R. E., and Coauthors, 2014: Deformation, warming and softening of Greenland’s ice by
579 refreezing meltwater. *Nature Geoscience*, **7** (7), 497–502.
- 580 Bennartz, R., and Coauthors, 2013: July 2012 Greenland melt extent enhanced by low-level liquid
581 clouds. *Nature*, **496** (7443), 83–86.

582 Bromwich, D. H., J. P. Nicolas, A. J. Monaghan, M. A. Lazzara, L. M. Keller, G. A. Weidner,
 583 and A. B. Wilson, 2013: Central West Antarctica among the most rapidly warming regions on
 584 Earth. *Nature Geoscience*, **6** (2), 139–145.

585 Bromwich, D. H., and Coauthors, 2012: Tropospheric clouds in Antarctica. *Reviews of Geo-*
 586 *physics*, **50** (1).

587 Cesana, G., J. Kay, H. Chepfer, J. English, and G. de Boer, 2012: Ubiquitous low-level liquid-
 588 containing Arctic clouds: New observations and climate model constraints from CALIPSO-
 589 GOCCP. *Geophysical Research Letters*, **39** (20).

590 Das, S. B., and R. B. Alley, 2008: Rise in frequency of surface melting at Siple Dome through the
 591 Holocene: Evidence for increasing marine influence on the climate of West Antarctica. *Journal*
 592 *of Geophysical Research: Atmospheres*, **113** (D2).

593 Das, S. B., I. Joughin, M. D. Behn, I. M. Howat, M. A. King, D. Lizarralde, and M. P. Bhatia,
 594 2008: Fracture propagation to the base of the Greenland Ice Sheet during supraglacial lake
 595 drainage. *Science*, **320** (5877), 778–781.

596 DeConto, R. M., and D. Pollard, 2016: Contribution of Antarctica to past and future sea-level rise.
 597 *Nature*, **531** (7596), 591–597.

598 Dee, D., and Coauthors, 2011: The ERA-Interim reanalysis: Configuration and performance of
 599 the data assimilation system. *Quarterly Journal of the Royal Meteorological Society*, **137** (656),
 600 553–597.

601 Enderlin, E. M., I. M. Howat, S. Jeong, M.-J. Noh, J. H. Angelen, and M. R. van den Broeke,
 602 2014: An improved mass budget for the Greenland ice sheet. *Geophysical Research Letters*,
 603 **41** (3), 866–872.

604 Frieler, K., and Coauthors, 2015: Consistent evidence of increasing Antarctic accumulation with
 605 warming. *Nature Climate Change*, **5**, 348–352.

606 Fudge, T., and Coauthors, 2016: Variable relationship between accumulation and temperature in
 607 West Antarctica for the past 31,000 years. *Geophysical Research Letters*, **43** (8), 3795–3803.

608 Gorodetskaya, I., and Coauthors, 2015: Cloud and precipitation properties from ground-based
 609 remote-sensing instruments in East Antarctica. *The Cryosphere*, **9** (1), 285–304.

610 Grenfell, T. C., S. G. Warren, and P. C. Mullen, 1994: Reflection of solar radiation by the Antarc-
 611 tic snow surface at ultraviolet, visible, and near-infrared wavelengths. *Journal of Geophysical*
 612 *Research: Atmospheres*, **99** (D9), 18 669–18 684.

613 Illingworth, A., and Coauthors, 2015: The EarthCARE satellite: The next step forward in global
 614 measurements of clouds, aerosols, precipitation, and radiation. *Bulletin of the American Meteoro-*
 615 *logical Society*, **96** (8), 1311–1332.

616 Intrieri, J., C. Fairall, M. Shupe, P. Persson, E. Andreas, P. Guest, and R. Moritz, 2002: An annual
 617 cycle of Arctic surface cloud forcing at SHEBA. *Journal of Geophysical Research*, **107** (C10).

618 Johanson, C. M., and Q. Fu, 2007: Antarctic atmospheric temperature trend patterns from satellite
 619 observations. *Geophysical Research Letters*, **34** (12).

620 Joughin, I., B. E. Smith, and B. Medley, 2014: Marine ice sheet collapse potentially under way for
 621 the Thwaites Glacier Basin, West Antarctica. *Science*, **344** (6185), 735–738.

622 Kato, S., N. G. Loeb, D. A. Rutan, F. G. Rose, S. Sun-Mack, W. F. Miller, and Y. Chen, 2012:
 623 Uncertainty estimate of surface irradiances computed with MODIS-, CALIPSO-, and CloudSat-
 624 derived cloud and aerosol properties. *Surveys in Geophysics*, **33** (3-4), 395–412.

625 Kato, S., S. Sun-Mack, W. F. Miller, F. G. Rose, Y. Chen, P. Minnis, and B. A. Wielicki, 2010:
 626 Relationships among cloud occurrence frequency, overlap, and effective thickness derived from
 627 CALIPSO and CloudSat merged cloud vertical profiles. *Journal of Geophysical Research: At-*
 628 *mospheres*, **115** (D4).

629 Kato, S., and Coauthors, 2011: Improvements of top-of-atmosphere and surface irradiance compu-
 630 tations with CALIPSO-, CloudSat-, and MODIS-derived cloud and aerosol properties. *Journal*
 631 *of Geophysical Research: Atmospheres*, **116** (D19).

632 King, J., and Coauthors, 2015: Validation of the summertime surface energy budget of Larsen C
 633 Ice Shelf (Antarctica) as represented in three high-resolution atmospheric models. *Journal of*
 634 *Geophysical Research: Atmospheres*, **120** (4), 1335–1347.

635 Klein, S. A., and Coauthors, 2009: Intercomparison of model simulations of mixed-phase clouds
 636 observed during the ARM Mixed-Phase Arctic Cloud Experiment. I: Single-layer cloud. *Quar-*
 637 *terly Journal of the Royal Meteorological Society*, **135** (641), 979–1002.

638 Kopp, R. E., and Coauthors, 2016: Temperature-driven global sea-level variability in the Common
 639 Era. *Proceedings of the National Academy of Sciences*, 201517056.

640 Lawson, R. P., and A. Gettelman, 2014: Impact of Antarctic mixed-phase clouds on climate.
 641 *Proceedings of the National Academy of Sciences*, **111** (51), 18 156–18 161.

642 Lenaerts, J. T., M. Vizcaino, J. Fyke, L. Kampenhout, and M. R. van den Broeke, 2016: Present-
 643 day and future Antarctic ice sheet climate and surface mass balance in the Community Earth
 644 System Model. *Climate Dynamics*, 1–15.

645 Lohmann, U., J. Henneberger, O. Henneberg, J. Fugal, J. Bühl, and Z. Kanji, 2016: Persistence of
 646 orographic mixed-phase clouds. *Geophysical Research Letters*, **43** (19).

647 Lubin, D., B. H. Kahn, M. A. Lazzara, P. Rowe, and V. P. Walden, 2015: Variability in AIRS-
648 retrieved cloud amount and thermodynamic phase over West versus East Antarctica influenced
649 by the SAM. *Geophysical Research Letters*, **42** (4), 1259–1267.

650 Mercer, J. H., 1978: West Antarctic ice sheet and CO₂ greenhouse effect - A threat of disaster.
651 *Nature*, **271** (5643), 321–325.

652 Miller, N. B., M. D. Shupe, C. J. Cox, V. P. Walden, D. D. Turner, and K. Steffen, 2015: Cloud
653 radiative forcing at Summit, Greenland. *Journal of Climate*, **28** (15), 6267–6280.

654 Nghiem, S., K. Steffen, G. Neumann, and R. Huff, 2007: Snow accumulation and snowmelt
655 monitoring in Greenland and Antarctica. *Dynamic Planet*, Springer, 31–38.

656 Nicolas, J. P., and D. H. Bromwich, 2011: Climate of West Antarctica and Influence of Marine
657 Air Intrusions. *Journal of Climate*, **24** (1), 49–67.

658 Nicolas, J. P., and D. H. Bromwich, 2014: New Reconstruction of Antarctic Near-Surface Temper-
659 atures: Multidecadal Trends and Reliability of Global Reanalyses. *Journal of Climate*, **27** (21),
660 8070–8093.

661 Nicolas, J. P., and Coauthors, 2017: January 2016 extensive summer melt in West Antarctica
662 favored by strong El Niño. *Nature Communications*.

663 Niwano, M., T. Aoki, S. Matoba, S. Yamaguchi, T. Tanikawa, K. Kuchiki, and H. Motoyama,
664 2015: Numerical simulation of extreme snowmelt observed at the SIGMA-A site, northwest
665 Greenland, during summer 2012. *The Cryosphere*, **9** (3), 971–988.

666 Ohmura, A., E. G. Dutton, B. Forgan, C. Frohlich, and Coauthors, 1998: Baseline Surface Radi-
667 ation Network (BSRN/WCRP): New precision radiometry for climate research. *Bulletin of the*
668 *American Meteorological Society*, **79** (10), 2115.

Orsi, A. J., B. D. Cornuelle, and J. P. Severinghaus, 2012: Little Ice Age cold interval in West Antarctica: evidence from borehole temperature at the West Antarctic Ice Sheet (WAIS) divide. *Geophysical Research Letters*, **39** (9).

Paolo, F. S., H. A. Fricker, and L. Padman, 2015: Volume loss from Antarctic ice shelves is accelerating. *Science*, **348** (6232), 327–331.

Parish, T. R., and D. H. Bromwich, 1987: The surface windfield over the Antarctic ice sheets. *Nature*, **328** (6125), 51–54.

Ramanathan, V., R. Cess, E. Harrison, P. Minnis, B. Barkstrom, E. Ahmad, and D. Hartmann, 1989: Cloud-radiative forcing and climate: Results from the Earth Radiation Budget Experiment. *Science*, **243** (4887).

Raphael, M., and Coauthors, 2016: The Amundsen Sea Low: variability, change, and impact on Antarctic climate. *Bulletin of the American Meteorological Society*, **97** (1), 111–121.

Reusch, D. B., and R. B. Alley, 2004: A 15-year West Antarctic climatology from six automatic weather station temperature and pressure records. *Journal of Geophysical Research: Atmospheres*, **109** (D4).

Rignot, E., G. Casassa, P. Gogineni, W. Krabill, A. Rivera, and R. Thomas, 2004: Accelerated ice discharge from the Antarctic Peninsula following the collapse of Larsen B ice shelf. *Geophysical Research Letters*, **31** (18).

Rignot, E., J. Mouginot, M. Morlighem, H. Seroussi, and B. Scheuchl, 2014: Widespread, rapid grounding line retreat of Pine Island, Thwaites, Smith, and Kohler glaciers, West Antarctica, from 1992 to 2011. *Geophysical Research Letters*, **41** (10), 3502–3509.

690 Scambos, T. A., J. A. Bohlander, C. A. Shuman, and P. Skvarca, 2004: Glacier acceleration and
 691 thinning after ice shelf collapse in the Larsen B embayment, Antarctica. *Geophysical Research*
 692 *Letters*, **31** (18).

693 Scambos, T. A., C. Hulbe, M. Fahnestock, and J. Bohlander, 2000: The link between climate
 694 warming and break-up of ice shelves in the Antarctic Peninsula. *Journal of Glaciology*, **46** (154),
 695 516–530.

696 Schneider, D. P., C. Deser, and Y. Okumura, 2012: An assessment and interpretation of the ob-
 697 served warming of west antarctica in the austral spring. *Climate Dynamics*, **38** (1-2), 323–347.

698 Schneider, D. P., and E. J. Steig, 2008: Ice cores record significant 1940s Antarctic warmth re-
 699 lated to tropical climate variability. *Proceedings of the National Academy of Sciences*, **105** (34),
 700 12 154–12 158.

701 Scott, R. C., and D. Lubin, 2014: Mixed-phase cloud radiative properties over Ross Island, Antarc-
 702 tica: The influence of various synoptic-scale atmospheric circulation regimes. *Journal of Geo-*
 703 *physical Research: Atmospheres*, **119** (11), 6702–6723.

704 Scott, R. C., and D. Lubin, 2016: Unique manifestations of mixed-phase cloud microphysics over
 705 Ross Island and the Ross Ice Shelf, Antarctica. *Geophysical Research Letters*, **43**.

706 Seefeldt, M. W., and J. J. Cassano, 2008: An analysis of low-level jets in the greater Ross Ice Shelf
 707 region based on numerical simulations. *Monthly Weather Review*, **136** (11), 4188–4205.

708 Shepherd, A., and Coauthors, 2012: A Reconciled Estimate of Ice-Sheet Mass Balance. *Science*,
 709 **338** (6111), 1183–1189.

710 Shupe, M. D., 2011: Clouds at Arctic atmospheric observatories. Part II: Thermodynamic phase
 711 characteristics. *Journal of Applied Meteorology and Climatology*, **50** (3), 645–661.

712 Shupe, M. D., and J. M. Intrieri, 2004: Cloud radiative forcing of the Arctic surface: The influence
 713 of cloud properties, surface albedo, and solar zenith angle. *Journal of Climate*, **17 (3)**, 616–628.

714 Shupe, M. D., and Coauthors, 2013: High and dry: New observations of tropospheric and cloud
 715 properties above the Greenland Ice Sheet. *Bulletin of the American Meteorological Society*,
 716 **94 (2)**, 169–186.

717 Spinhirne, J., S. Palm, and W. Hart, 2005: Antarctica cloud cover for October 2003 from GLAS
 718 satellite lidar profiling. *Geophysical Research Letters*, **32 (22)**.

719 Steig, E. J., and Coauthors, 2013: Recent climate and ice-sheet changes in West Antarctica com-
 720 pared with the past 2,000 years. *Nature Geoscience*, **6 (5)**, 372–375.

721 Stephens, G. L., and Coauthors, 2002: The Cloudsat mission and the A-Train: A new dimension of
 722 space-based observations of clouds and precipitation. *Bulletin of the American Meteorological*
 723 *Society*, **83 (12)**, 1771–1790.

724 Stroeve, J., J. E. Box, F. Gao, S. Liang, A. Nolin, and C. Schaaf, 2005: Accuracy assessment of the
 725 MODIS 16-day albedo product for snow: comparisons with Greenland in situ measurements.
 726 *Remote Sensing of Environment*, **94 (1)**, 46–60.

727 Stroeve, J., J. E. Box, Z. Wang, C. Schaaf, and A. Barrett, 2013: Re-evaluation of MODIS MCD43
 728 Greenland albedo accuracy and trends. *Remote Sensing of Environment*, **138**, 199–214.

729 Tedesco, M., W. Abdalati, and H. Zwally, 2007: Persistent surface snowmelt over Antarctica
 730 (1987-2006) from 19.35 GHz brightness temperatures. *Geophysical Research Letters*, **34 (18)**.

731 Thomas, E. R., T. J. Bracegirdle, J. Turner, and E. W. Wolff, 2013: A 308 year record of climate
 732 variability in West Antarctica. *Geophysical Research Letters*, **40 (20)**, 5492–5496.

733 Thomas, E. R., J. S. Hosking, R. R. Tuckwell, R. Warren, and E. Ludlow, 2015: Twentieth century
 734 increase in snowfall in coastal West Antarctica. *Geophysical Research Letters*, **42** (21), 9387–
 735 9393.

736 Tjernström, M., and Coauthors, 2015: Warm-air advection, air mass transformation and fog causes
 737 rapid ice melt. *Geophysical Research Letters*, **42** (13), 5594–5602.

738 Town, M. S., and V. P. Walden, 2009: Surface energy budget over the South Pole and turbulent heat
 739 fluxes as a function of an empirical bulk Richardson number. *Journal of Geophysical Research:*
 740 *Atmospheres*, **114** (D22).

741 Town, M. S., V. P. Walden, and S. G. Warren, 2005: Spectral and broadband longwave down-
 742 welling radiative fluxes, cloud radiative forcing, and fractional cloud cover over the South Pole.
 743 *Journal of Climate*, **18** (20), 4235–4252.

744 Trusel, L. D., K. E. Frey, S. B. Das, K. B. Karnauskas, P. K. Munneke, E. Van Meijgaard, and
 745 M. R. van den Broeke, 2015: Divergent trajectories of Antarctic surface melt under two twenty-
 746 first-century climate scenarios. *Nature Geoscience*.

747 van den Broeke, M. R., 2005: Strong surface melting preceded collapse of Antarctic Peninsula ice
 748 shelf. *Geophysical Research Letters*, **32** (12).

749 van den Broeke, M. R., E. Enderlin, I. Howat, P. Kuipers Munneke, B. Noël, W. J. van de Berg,
 750 E. van Meijgaard, and B. Wouters, 2016: On the recent contribution of the Greenland ice sheet
 751 to sea level change. *The Cryosphere Discussions*, **2016**, 1–26, doi:10.5194/tc-2016-123.

752 van Tricht, K., and Coauthors, 2016: Clouds enhance Greenland ice sheet meltwater runoff. *Nature*
 753 *Communications*, **7**.

Verlinden, K. L., D. W. Thompson, and G. L. Stephens, 2011: The three-dimensional distribution of clouds over the Southern Hemisphere high latitudes. *Journal of Climate*, **24** (22), 5799–5811.

Wang, Z., D. Vane, G. Stephens, and D. Reinke, 2013: Level 2 Combined Radar and Lidar Cloud Scenario Classification Product Process Description and Interface Control Document. *Jet Propulsion Laboratory California Institute of Technology*.

Winker, D. M., M. A. Vaughan, A. Omar, Y. Hu, K. A. Powell, Z. Liu, W. H. Hunt, and S. A. Young, 2009: Overview of the CALIPSO mission and CALIOP data processing algorithms. *Journal of Atmospheric and Oceanic Technology*, **26** (11), 2310–2323.

Zhang, D., Z. Wang, and D. Liu, 2010: A global view of midlevel liquid-layer topped stratiform cloud distribution and phase partition from CALIPSO and CloudSat measurements. *Journal of Geophysical Research: Atmospheres*, **115** (D4).

Zhang, T., K. Stamnes, and S. Bowling, 1996: Impact of clouds on surface radiative fluxes and snowmelt in the Arctic and subarctic. *Journal of Climate*, **9** (9), 2110–2123.

Zwally, H. J., W. Abdalati, T. Herring, K. Larson, J. Saba, and K. Steffen, 2002: Surface melt-induced acceleration of Greenland ice-sheet flow. *Science*, **297** (5579), 218–222.

Zwally, H. J., J. Li, J. W. Robbins, J. L. Saba, D. Yi, and A. C. Brenner, 2015: Mass gains of the Antarctic ice sheet exceed losses. *Journal of Glaciology*, **61** (230), 1019–1036.

771	LIST OF TABLES	
772	Table 1.	CloudSat-CALIPSO 2B-CLDCLASS-LIDAR cloud thermodynamic phase re-
773		trieval confidence flag statistics over Antarctica and the Southern Ocean. Val-
774		ues indicate the percentage (%) of retrievals having high confidence, that is, a
775		flag value greater than 5 (Wang et al. 2013). 36
776	Table 2.	C3M instantaneous all-sky surface LW↓ validation statistics at Antarctic BSRN
777		sites for each season, from 2007-2010. Units for bias are W m^{-2} 37
778	Table 3.	Comparison of monthly mean C3M all-sky LW↓ and SW↓ fluxes with BSRN
779		measurements, from 2007-2010. Units for bias are W m^{-2} 38
780	Table 4.	Mean December-January net surface radiative fluxes at WAIS Divide estimated
781		from satellites and measured during AWARE. The standard deviation is given
782		in parenthesis. All units are W m^{-2} 39

783 TABLE 1. CloudSat-CALIPSO 2B-CLDCLASS-LIDAR cloud thermodynamic phase retrieval confidence flag
784 statistics over Antarctica and the Southern Ocean. Values indicate the percentage (%) of retrievals having high
785 confidence, that is, a flag value greater than 5 (Wang et al. 2013).

	Spring (SON)	Summer (DJF)	Autumn (MAM)	Winter (JJA)
Ice	100	100	100	100
Mixed-phase	94.32	97.20	95.62	93.34
Liquid	100	100	100	100

786 TABLE 2. C3M instantaneous all-sky surface $LW\downarrow$ validation statistics at Antarctic BSRN sites for each
787 season, from 2007-2010. Units for bias are $W\ m^{-2}$.

	Antarctic BSRN			Neumayer			Syowa			Concordia		
	Bias	RMSE	Corr	Bias	RMSE	Corr	Bias	RMSE	Corr	Bias	RMSE	Corr
Spring (SON)	1.33	31.86	0.89	-3.83	30.71	0.79	-6.79	37.17	0.58	15.01	26.12	0.69
Summer (DJF)	0.98	32.57	0.90	0.04	29.46	0.70	-11.13	36.60	0.48	12.64	30.94	0.61
Autumn (MAM)	-4.50	32.84	0.90	-11.04	28.42	0.79	-9.51	40.86	0.59	9.87	23.67	0.74
Winter (JJA)	-2.29	33.30	0.88	-5.59	31.72	0.69	-11.55	41.87	0.59	10.32	22.77	0.72

788 TABLE 3. Comparison of monthly mean C3M all-sky LW↓ and SW↓ fluxes with BSRN measurements, from
789 2007-2010. Units for bias are W m^{-2} .

	Antarctic BSRN			Neumayer			Syowa			Concordia		
	Bias	RMSE	Corr	Bias	RMSE	Corr	Bias	RMSE	Corr	Bias	RMSE	Corr
LW↓	-0.69	12.37	0.98	-4.45	10.45	0.93	-8.01	11.72	0.93	13.33	15.11	0.90
SW↓	-13.16	36.90	0.97	-21.32	39.30	0.96	-1.50	28.40	0.97	-18.25	43.64	0.97

790 TABLE 4. Mean December-January net surface radiative fluxes at WAIS Divide estimated from satellites and
791 measured during AWARE. The standard deviation is given in parenthesis. All units are W m^{-2} .

	C3M	AWARE
net LW	-46.36 (38.82)	-46.18 (29.07)
net SW	66.87 (32.60)	59.25 (28.02)
net total	20.52 (26.06)	12.49 (17.63)

LIST OF FIGURES

792	Fig. 1.	Map of West Antarctica showing the terrain height at a 250 m interval. Initials show the location of the Amundsen Sea (AS), Amundsen Sea Embayment (ASE), Bellingshausen Sea (BS), Central Ice Divide (CID), Filchner Ice Shelf (FIS), Larsen C Ice Shelf (LCIS), and Marie Byrd Land (MBL). Dots on the inset map indicate the location of the WAIS Divide Ice Camp (green) and Neumayer (orange), Syowa (red), and Concordia Stations (blue).	42
793	Fig. 2.	C3M surface downwelling longwave irradiance ($LW\downarrow$) validation at BSRN sites in West and East Antarctica, for the period 2007-10. (top row) Scatterplots of the instantaneous C3M-modeled versus BSRN-measured $LW\downarrow$. The upper panels include the mean bias (Δ) [$W\ m^{-2}$], root-mean-square error (RMSE), Pearson linear correlation coefficient (r), and linear least squares regression curve as a blue dashed line. (bottom row) Distributions of the instantaneous (modeled-measured) irradiance error. The Antarctic BSRN category includes data from all three sites.	43
794	Fig. 3.	Seasonal cloud amount over WA from CloudSat-CALIPSO overlaid with mean horizontal circulation vectors at 700-mb from ERA-Interim, for (a) spring (SON), (b) summer (DJF), (c) autumn (MAM), and (d) winter (JJA) during 2007-10. The star in panel (b) marks the location of WAIS Divide. No satellite data are available poleward of $82^\circ S$.	44
795	Fig. 4.	Seasonal composites of the minus pressure vertical velocity, or omega, at 700-mb ($-\omega_{700}$) from ERA-Interim during (a) spring (SON), (b) summer (DJF), (c) autumn (MAM), and (d) winter (JJA), for the period 2007-10. Positive values depict upward motion.	45
796	Fig. 5.	Zonal transects of seasonal cloud incidence over WA along $77^\circ S$, for the period 2007-10. In each panel, cloud incidence is partitioned by thermodynamic phase: (top) ice, (middle) mixed-phase, and (bottom) liquid water. From left to right: Antarctic Plateau, Ross Sea, Marie Byrd Land, Ellsworth Land, Ronne-Filchner Ice Shelf, Weddell Sea, Queen Maud Land.	46
797	Fig. 6.	Same as Figure 5, but along $79^\circ S$. WAIS Divide is located in the middle of the transect at $248^\circ E$. From left to right: Transantarctic Mountains, northern Ross Ice Shelf, West Antarctic Ice Sheet, Ronne Ice Shelf, Berkner Island, Filchner Ice Shelf, Queen Maud Land.	47
800	Fig. 7.	Same as Figure 5, but along $81^\circ S$. From left to right: Transantarctic Mountains, Ross Ice Shelf, Siple Coast, Central Ice Divide, southern Ronne-Filchner Ice Shelf, Queen Maud Land.	48
801	Fig. 8.	Monthly cloud incidence over WA during the austral summer, from 2007-2010. As in Figs. 5-7, cloud incidence is partitioned by thermodynamic phase. Major rows correspond to latitude bands (top) 77° , (middle) 79° , and (bottom) $81^\circ S$, whereas columns correspond to (left) December, (middle) January, (right) February.	49
802	Fig. 9.	Annual cycle and monthly variability in net longwave, shortwave, and all-wave radiative fluxes (left) over the entire WAIS, and (right) at the WAIS Divide Ice Camp. Green diamonds show the average fluxes measured at WAIS Divide during AWARE, from 4 December 2015 to 18 January 2016. Monthly radiant flux distributions are illustrated by box-and-whisker plots. The mean annual cycle is shown as circles connected by a black curve, the interior line indicates the median, boxes show the 25th and 75th percentiles, and whiskers extend to the 5th and 95th percentiles.	50
803	Fig. 10.	Same as Fig. 9, but for the net longwave, shortwave, and all-wave CRE.	51

835	Fig. 11.	Seasonal means of the surface longwave CRE [W m^{-2}] over WA calculated from CALIPSO,	
836		CloudSat, and MODIS cloud observations during (a) spring (SON), (b) summer (DJF), (c)	
837		autumn (MAM), and (d) winter (JJA), for the period 2007-2010.	52
838	Fig. 12.	Same as Figure 11, but the for surface shortwave CRE [W m^{-2}].	53
839	Fig. 13.	Same as Figure 11, but for the surface all-wave CRE [W m^{-2}].	54

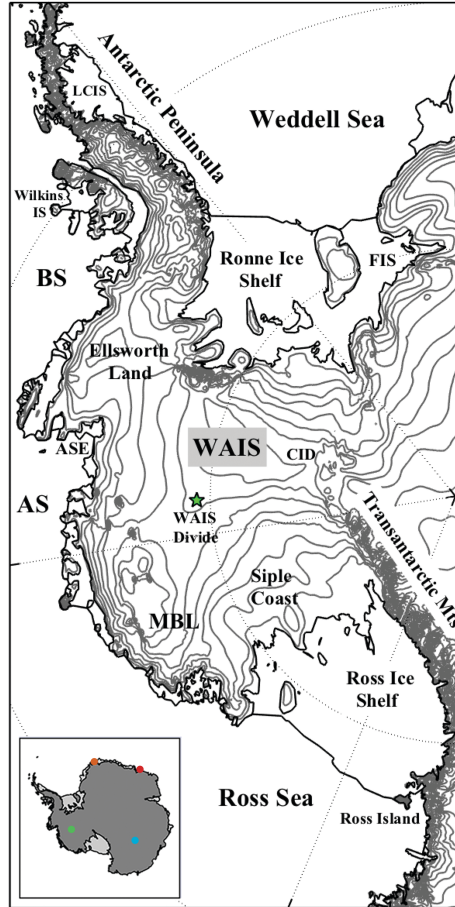


FIG. 1. Map of West Antarctica showing the terrain height at a 250 m interval. Initials show the location of the Amundsen Sea (AS), Amundsen Sea Embayment (ASE), Bellingshausen Sea (BS), Central Ice Divide (CID), Filchner Ice Shelf (FIS), Larsen C Ice Shelf (LCIS), and Marie Byrd Land (MBL). Dots on the inset map indicate the location of the WAIS Divide Ice Camp (green) and Neumayer (orange), Syowa (red), and Concordia Stations (blue).

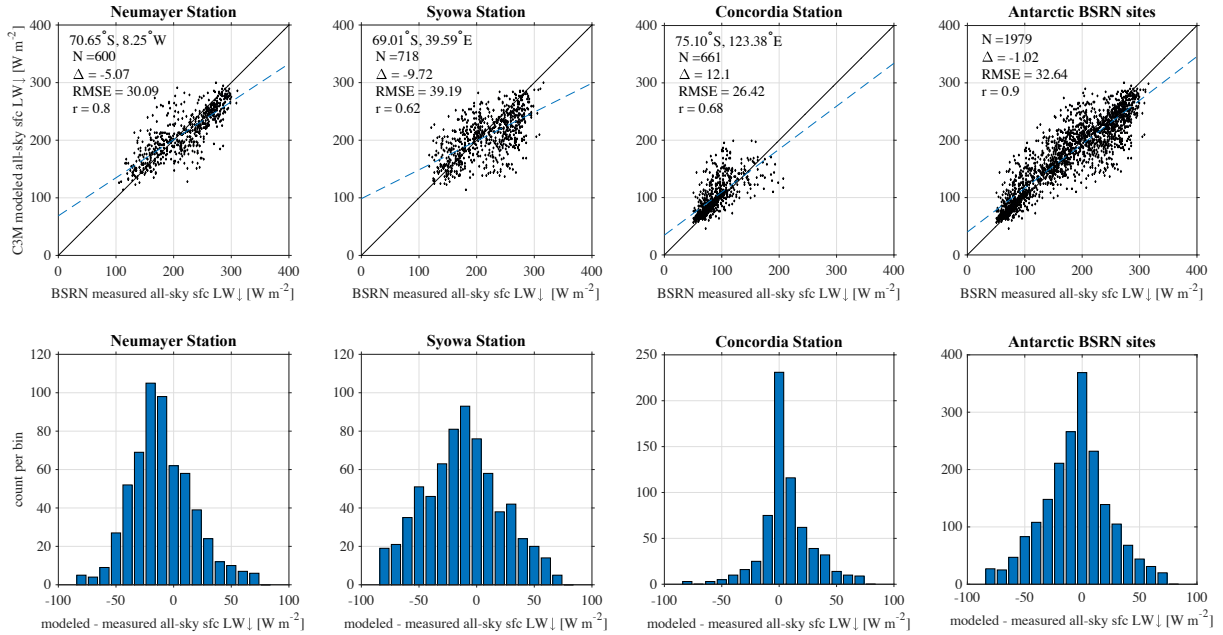
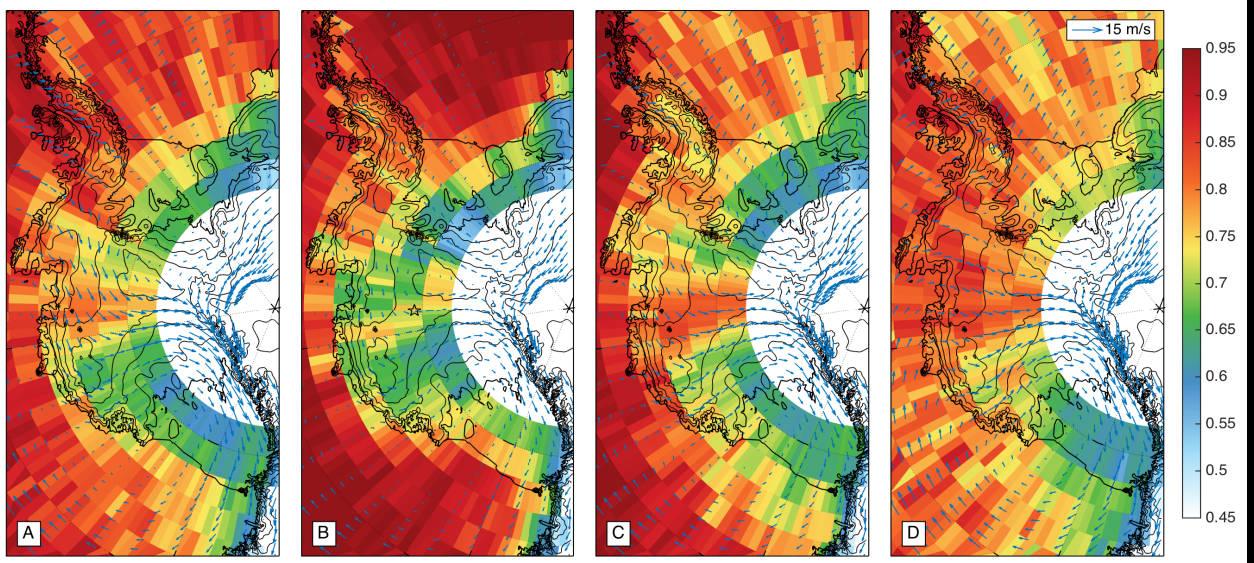
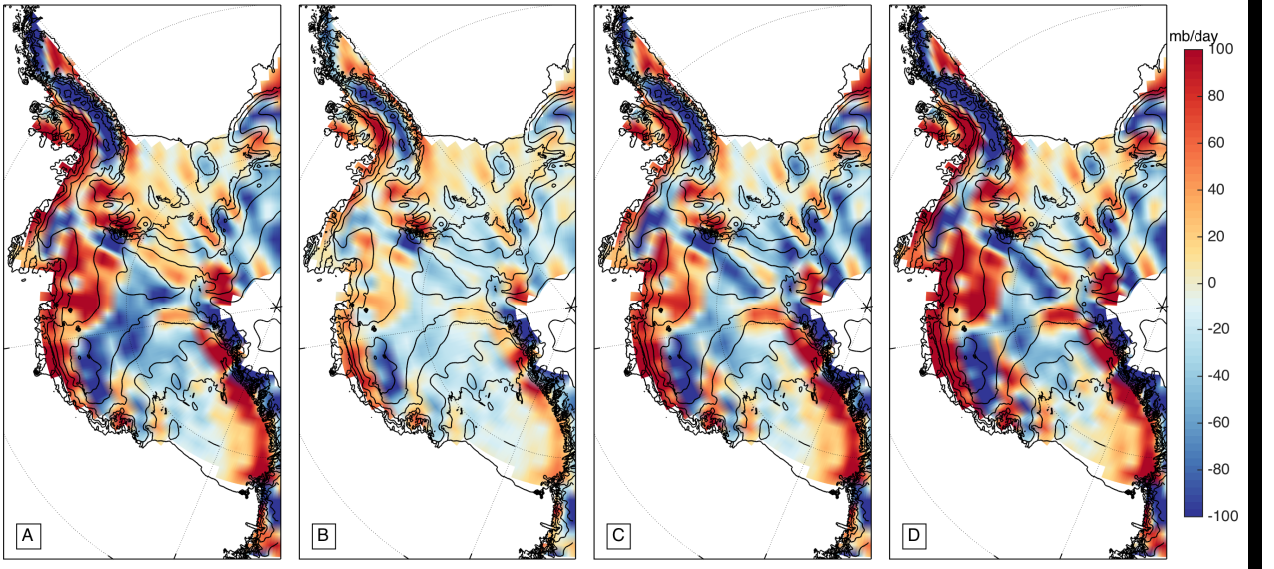


FIG. 2. C3M surface downwelling longwave irradiance ($LW\downarrow$) validation at BSRN sites in West and East Antarctica, for the period 2007-10. (top row) Scatterplots of the instantaneous C3M-modeled versus BSRN-measured $LW\downarrow$. The upper panels include the mean bias (Δ) [$W\ m^{-2}$], root-mean-square error (RMSE), Pearson linear correlation coefficient (r), and linear least squares regression curve as a blue dashed line. (bottom row) Distributions of the instantaneous (modeled-measured) irradiance error. The Antarctic BSRN category includes data from all three sites.



851 FIG. 3. Seasonal cloud amount over WA from CloudSat-CALIPSO overlaid with mean horizontal circulation
 852 vectors at 700-mb from ERA-Interim, for (a) spring (SON), (b) summer (DJF), (c) autumn (MAM), and (d)
 853 winter (JJA) during 2007-10. The star in panel (b) marks the location of WAIS Divide. No satellite data are
 854 available poleward of 82°S .



855 FIG. 4. Seasonal composites of the minus pressure vertical velocity, or omega, at 700-mb ($-\omega_{700}$) from ERA-
 856 Interim during (a) spring (SON), (b) summer (DJF), (c) autumn (MAM), and (d) winter (JJA), for the period
 857 2007-10. Positive values depict upward motion.

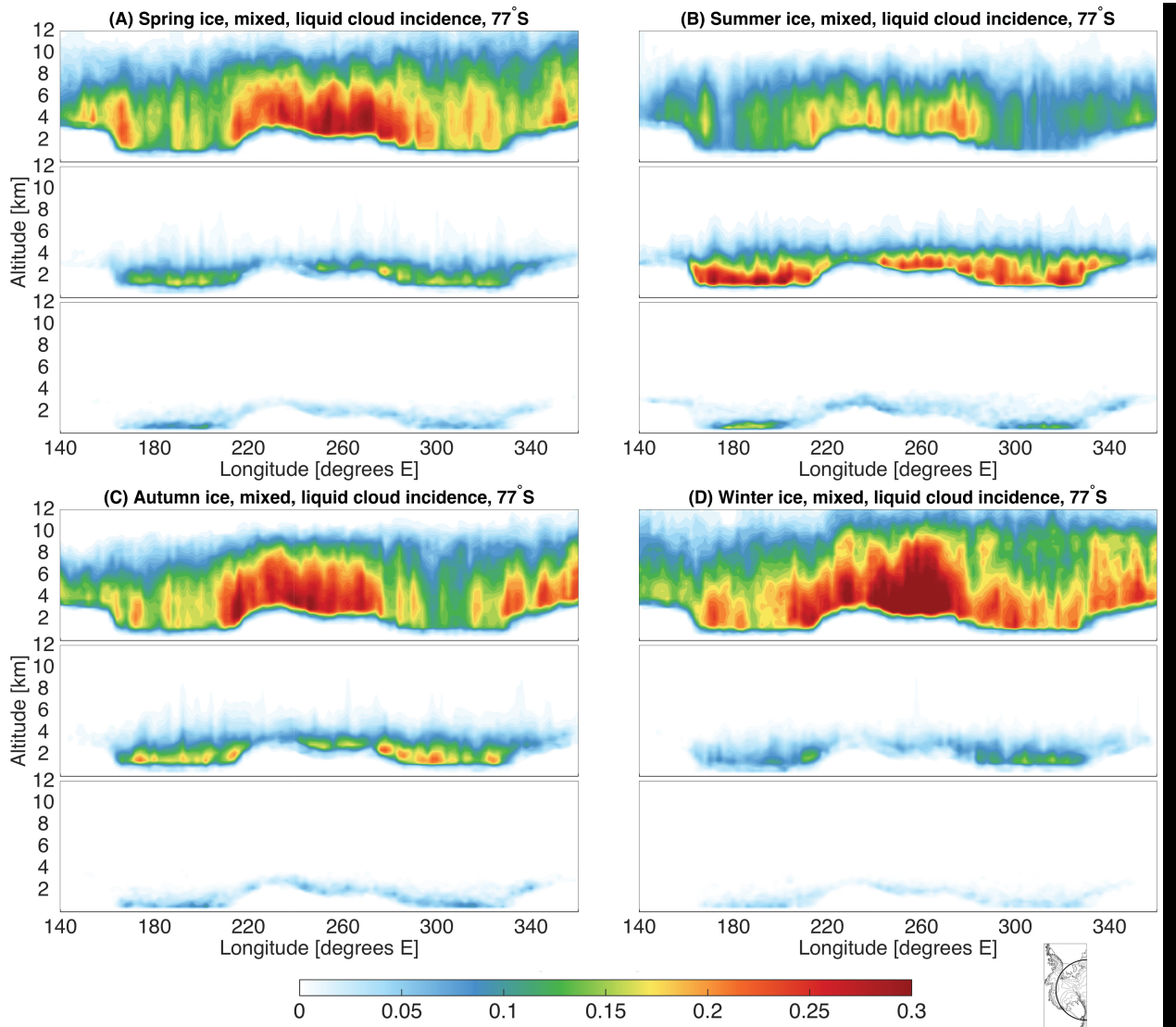


FIG. 5. Zonal transects of seasonal cloud incidence over WA along 77°S, for the period 2007-10. In each panel, cloud incidence is partitioned by thermodynamic phase: (top) ice, (middle) mixed-phase, and (bottom) liquid water. From left to right: Antarctic Plateau, Ross Sea, Marie Byrd Land, Ellsworth Land, Ronne-Filchner Ice Shelf, Weddell Sea, Queen Maud Land.

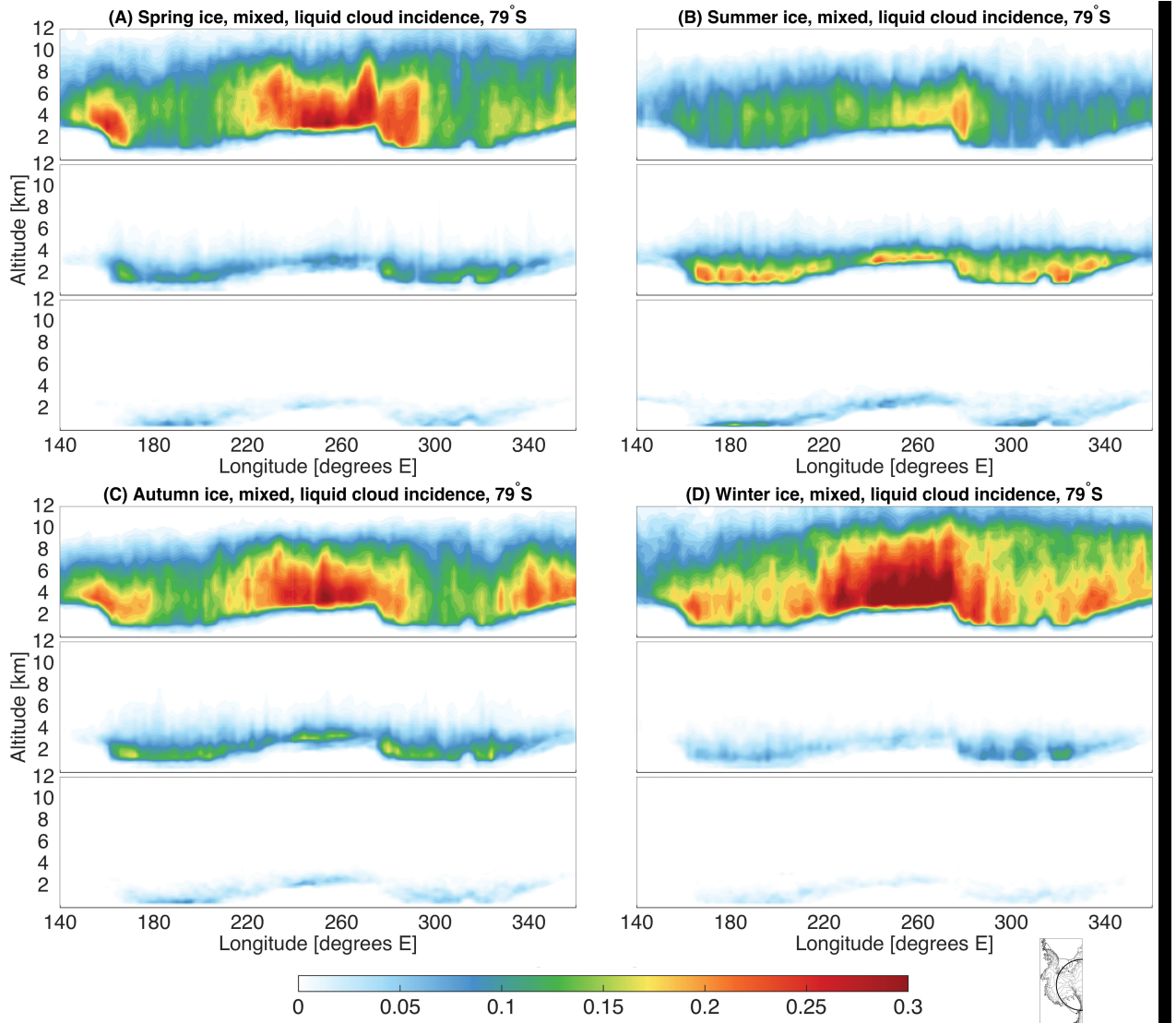


FIG. 6. Same as Figure 5, but along 79°S. WAIS Divide is located in the middle of the transect at 248°E. From left to right: Transantarctic Mountains, northern Ross Ice Shelf, West Antarctic Ice Sheet, Ronne Ice Shelf, Berkner Island, Filchner Ice Shelf, Queen Maud Land.

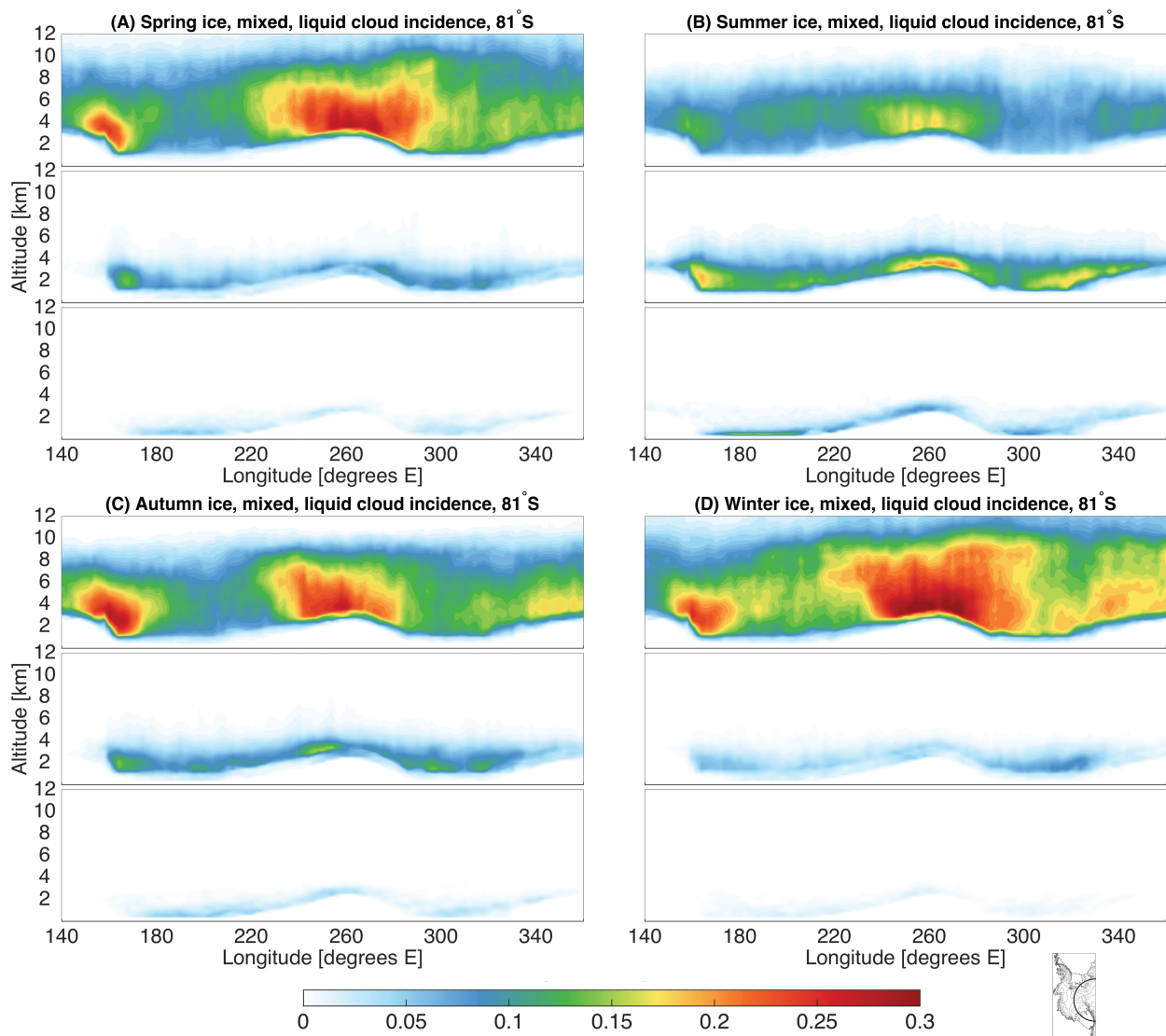


FIG. 7. Same as Figure 5, but along 81°S. From left to right: Transantarctic Mountains, Ross Ice Shelf, Siple Coast, Central Ice Divide, southern Ronne-Filchner Ice Shelf, Queen Maud Land.

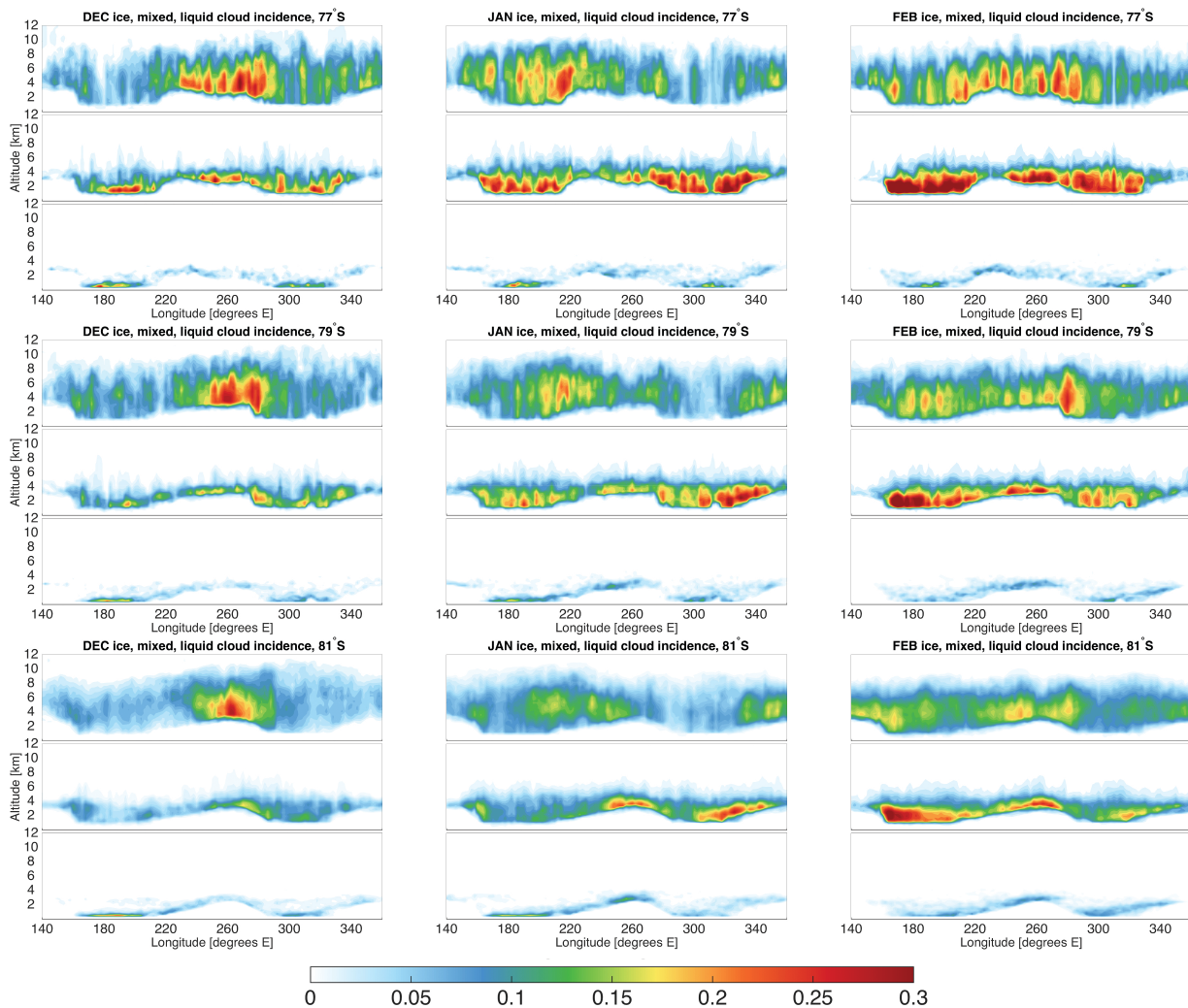


FIG. 8. Monthly cloud incidence over WA during the austral summer, from 2007-2010. As in Figs. 5-7, cloud incidence is partitioned by thermodynamic phase. Major rows correspond to latitude bands (top) 77, (middle) 79, and (bottom) 81°S, whereas columns correspond to (left) December, (middle) January, (right) February.

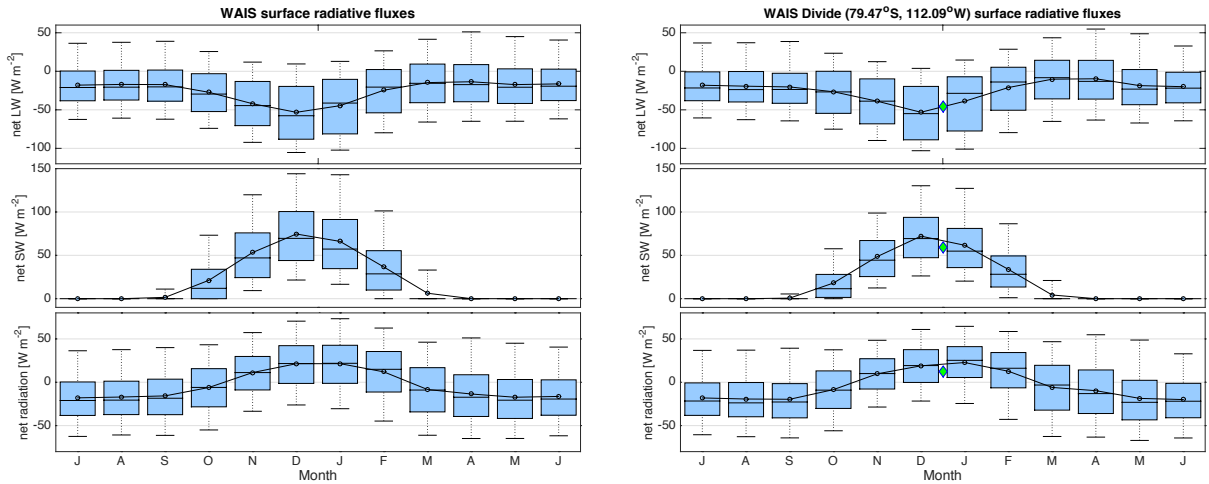


FIG. 9. Annual cycle and monthly variability in net longwave, shortwave, and all-wave radiative fluxes (left) over the entire WAIS, and (right) at the WAIS Divide Ice Camp. Green diamonds show the average fluxes measured at WAIS Divide during AWARE, from 4 December 2015 to 18 January 2016. Monthly radiant flux distributions are illustrated by box-and-whisker plots. The mean annual cycle is shown as circles connected by a black curve, the interior line indicates the median, boxes show the 25th and 75th percentiles, and whiskers extend to the 5th and 95th percentiles.

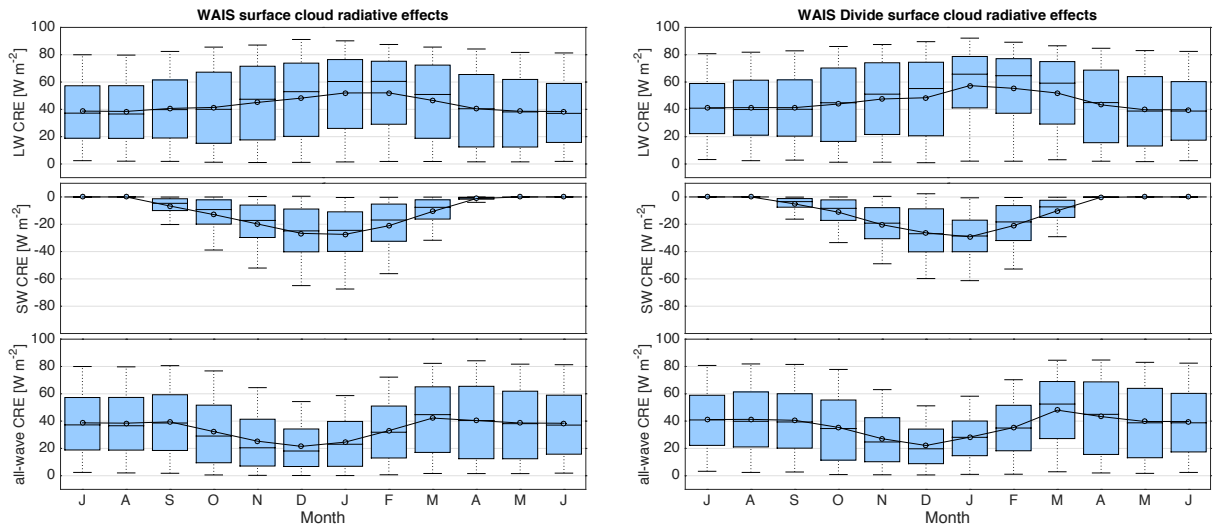
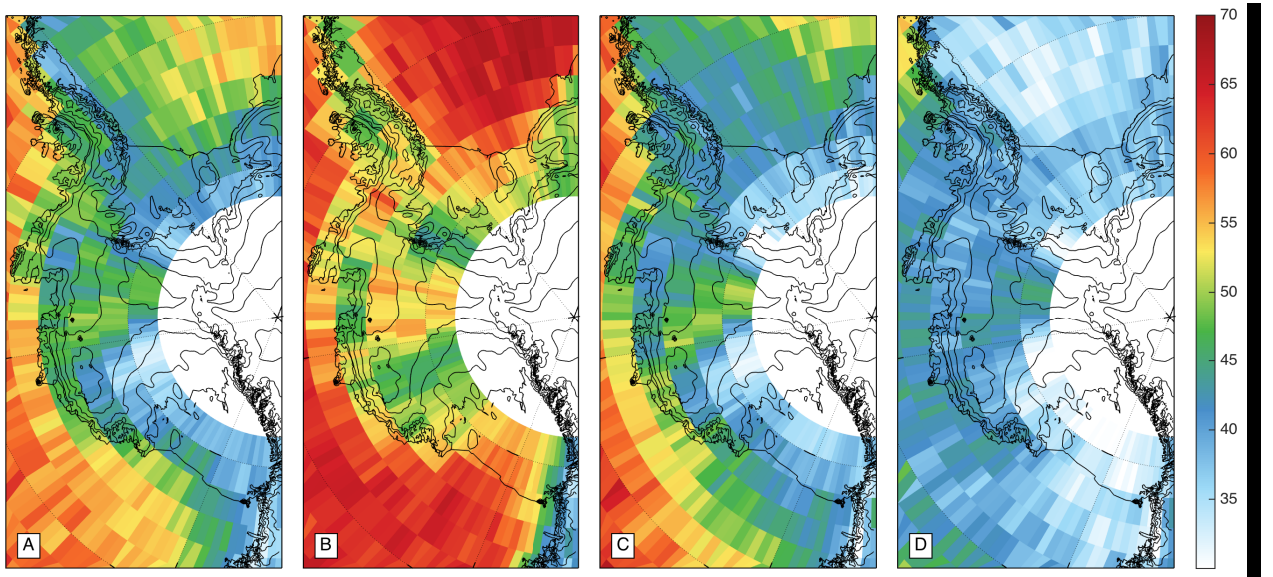


FIG. 10. Same as Fig. 9, but for the net longwave, shortwave, and all-wave CRE.



876 FIG. 11. Seasonal means of the surface longwave CRE [W m⁻²] over WA calculated from CALIPSO, Cloud-
 877 Sat, and MODIS cloud observations during (a) spring (SON), (b) summer (DJF), (c) autumn (MAM), and (d)
 878 winter (JJA), for the period 2007-2010.

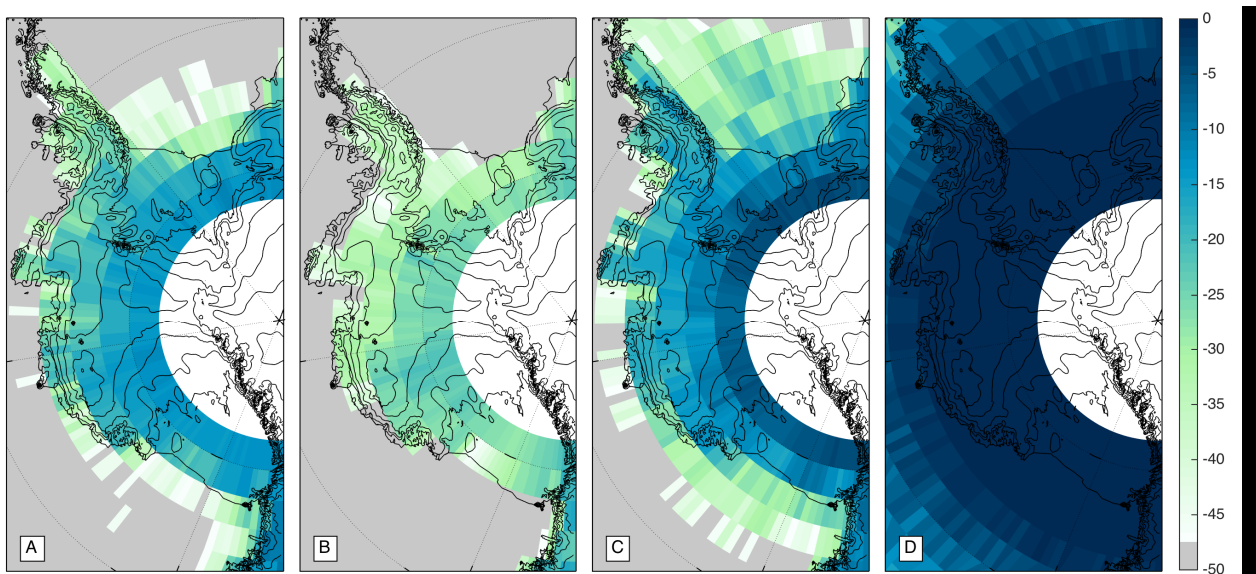


FIG. 12. Same as Figure 11, but the for surface shortwave CRE [W m⁻²].

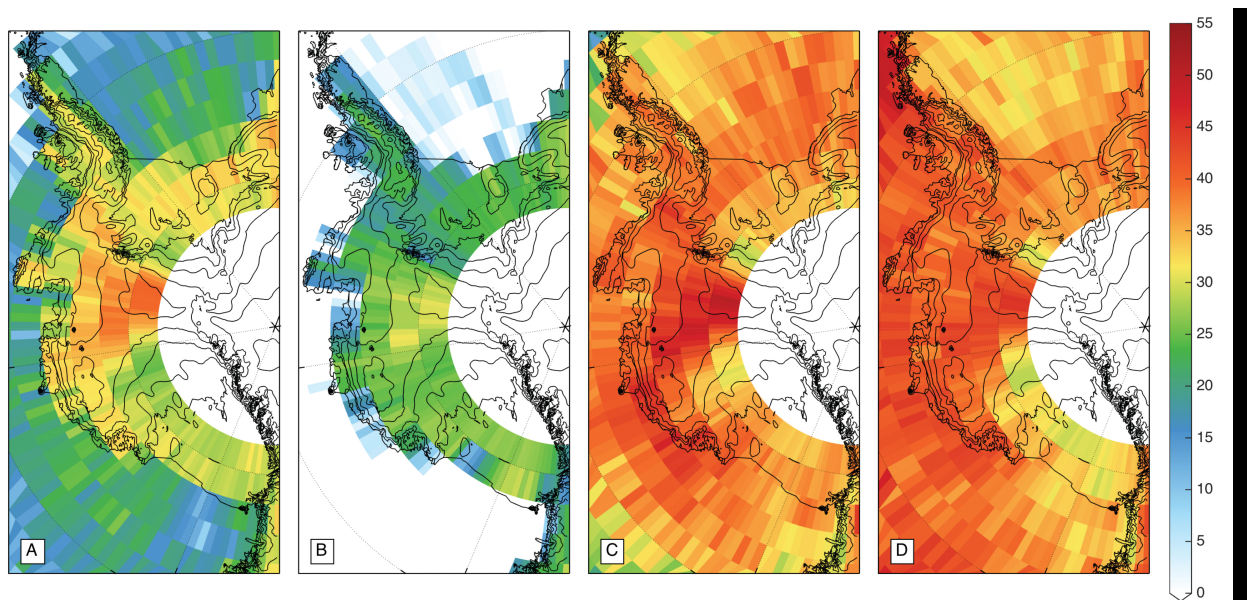


FIG. 13. Same as Figure 11, but for the surface all-wave CRE [W m^{-2}].